

---

**1 Local wind regime induced by giant linear dunes:  
2 comparison of ERA5 re-analysis with surface  
3 measurements**

**4 Cyril Gadal · Pauline Delorme ·  
5 Clément Narteau · Giles F.S. Wiggs ·  
6 Matthew Baddock · Joanna M. Nield ·  
7 Philippe Claudin**

**8**  
**9 Received: DD Month YEAR / Accepted: DD Month YEAR**

**10 Abstract**

**11** Emergence and growth of sand dunes results from the dynamic interaction be-  
**12** tween topography, wind flow and sediment transport. While feedbacks between  
**13** these variables are well studied at the scale of a single dune, the average effect  
**14** of a periodic dune pattern on atmospheric flows remains poorly constrained  
**15** due to a lack of data in major sand seas. Here, we compare field measurements  
**16** of surface wind data to the predictions of the ERA5-Land climate reanalysis at  
**17** four locations in Namibia, including within the giant-dune field of the Namib  
**18** sand sea. In the desert plains to the north of the sand sea, observations and  
**19** predictions agree well. This is also the case in the interdune areas of the sand  
**20** sea, except for the weak winds blowing at night, which exhibit additional com-

---

C. Gadal

Institut de Mécanique des Fluides de Toulouse, Université de Toulouse Paul Sabatier, CNRS,  
Toulouse INP-ENSEEIHT, Toulouse, France. E-mail: cyril.gadal@imft.fr

P. Delorme

School of Geography and Environmental Science, University of Southampton, Southampton,  
UK.

C. Narteau

Institut de Physique du Globe de Paris, Université de Paris, CNRS, Paris, France.

G. Wiggs

School of Geography and the Environment, University of Oxford, Oxford, UK.

M. Baddock

Geography and Environment, Loughborough University, Loughborough, UK.

J.M. Nield

School of Geography and Environmental Science, University of Southampton, Southampton,  
UK.

P. Claudin

Physique et Mécanique des Milieux Hétérogènes, CNRS, ESPCI Paris, PSL Research  
University, Université de Paris, Sorbonne Université, Paris, France. E-mail:  
philippe.claudin@espci.fr

ponents aligned with the giant dune orientation, which are not predicted by the ERA5-Land reanalysis. We quantify these similarities and differences and provide a physical understanding of the relevant aerodynamical regimes to relate them to the daily cycle of the turbulent atmospheric boundary layer over a dune pattern of given wavelength. We conclude by identifying the conditions under which the ERA5-Land reanalysis data can reliably be used to study dune morphodynamics. We also propose that, in multidirectional wind regimes, deflections of specific winds by giant dunes could explain the occurrence of secondary dune patterns with a different orientation to the primary structures between which they develop.

**Keywords** Atmospheric boundary layer · Sand dunes · Fluid-structure interactions

---

**33 1 Introduction**

34 The description of turbulent flows over a complex topography is a rich and  
35 active subject, that is relevant for a large variety of different environmental  
36 systems (Finnigan et al. 2020). For example, the flow over hills is of primary  
37 interest for wind power, meteorological and air pollution phenomena (Taylor  
38 et al. 1987). The properties of these flows are also key to the understanding of  
39 the formation of ocean surface wind-driven waves (Sullivan and McWilliams  
40 2010), dissolution bedforms (Claudin et al. 2017), or sedimentary ripples and  
41 dunes (Charru et al. 2013; Courrech du Pont 2015). Importantly, the tropo-  
42 sphere presents a vertical structure, with a lower convective boundary layer,  
43 of typical kilometer-scale thickness, capped by a stably stratified region (Stull  
44 1988). The largest topographic obstacles, such as mountains can therefore  
45 interact with this upper region, and lead to internal wave generation or signif-  
46 icant wind disturbances, such as lee-side downslope winds (Durran 1990).

47 Focusing on the wind close to the surface, two related topographic feed-  
48 backs on the windflow over dunes can be commented on separately. First is  
49 the effect on wind speed with documented flow acceleration on upwind slopes  
50 (Weaver and Wiggs 2011) and deceleration on downwind slopes (Baddock  
51 et al. 2007), with a speed-up factor essentially proportional to the obstacle  
52 aspect ratio (Jackson and Hunt 1975). Importantly, the velocity maximum is  
53 typically shifted upwind of the obstacle crest. This behaviour has been the-  
54oretically predicted by means of asymptotic analysis of a neutrally stratified  
55 boundary-layer flow over an obstacle of vanishing aspect ratio (Jackson and  
56 Hunt 1975; Mason and Sykes 1979; Sykes 1980; Hunt et al. 1988; Belcher and  
57 J.C.R. 1998). Experiments in flumes (Zilker et al. 1977; Zilker and Hanratty  
58 1979; Frederick and Hanratty 1988; Poggi et al. 2007), in wind tunnels (Gong  
59 and Ibbetson 1989; Finnigan et al. 1990; Gong et al. 1996) and in field condi-  
60 tions (Taylor and Teunissen 1987; Claudin et al. 2013; Fernando et al. 2019;  
61 Lü et al. 2021; Bristow et al. 2022), have also documented this effect. Inter-  
62 estingly, a similar behaviour exists for the pressure perturbation, but with a  
63 slight downwind shift for the pressure minimum (Claudin et al. 2021). The  
64 second effect, much less studied, is the flow deflection that occurs when the  
65 incident wind direction is not perpendicular to the ridge crest. While predicted  
66 to be small (less than 10°) in the linear regime valid for shallow topography  
67 (Gadal et al. 2019), significant flow steering has been reported in the field on  
68 the downwind side of steep enough obstacles, such as mountain ranges (Kim  
69 et al. 2000; Lewis et al. 2008; Fernando et al. 2019), well-developed sand dunes  
70 (Walker et al. 2009; Hesp et al. 2015; Walker et al. 2017; Smith et al. 2017),  
71 and valley topographies (Wiggs et al. 2002).

72 For practical reasons, wind measurement over sand dunes has been per-  
73 formed over rather small bedforms, typically a few meters high only (cor-  
74 responding to tens of meters long) (Wiggs et al. 1996). Giant dunes, with  
75 kilometer-scale wavelengths and heights of tens of meters, are more difficult  
76 to investigate although for several reasons they provide a choice configuration  
77 for the study of turbulent flows over a complex topography. First, one expects

78 larger wind disturbances for larger obstacles. Secondly, their large size makes  
79 them interact with the vertical structure of the atmosphere (Andreotti et al.  
80 2009). Third, they usually form large patterns in sand seas and thus behave as  
81 rather clean periodic perturbations, in contrast with isolated dunes. Finally,  
82 because the morphodynamics of aeolian bedforms are strongly dependent on  
83 the local wind regime (Livingstone and Warren 2019), one can expect to see the  
84 consequences of windflow disturbance by large dunes on neighbouring small  
85 dunes, in a similar manner to that reported for the effect of dunes on impact  
86 ripples (Howard 1977; Hood et al. 2021).

87 Atmospheric flows have been much studied at the desert-scale with climate  
88 reanalyses based on global atmospheric models (Blumberg and Greeley 1996;  
89 Livingstone et al. 2010; Ashkenazy et al. 2012; Jolivet et al. 2021; Hu et al.  
90 2021), such as ERA-40, ERA-Interim or ERA-5 (Uppala et al. 2005; Dee et al.  
91 2011; Hersbach et al. 2020). However, the spatial resolution (tens of kilometers)  
92 of these reanalyses implies average quantities that do not resolve the smaller  
93 scales, ranging from individual dunes to the border of mountains (Livingstone  
94 et al. 2010). Recently, the release of ERA5-Land has resolved this limitation  
95 by providing up to 70 years of hourly wind predictions at a 9 km spatial  
96 resolution (Muñoz-Sabater et al. 2021). However, its validity remains to be  
97 studied, especially in remote desert areas where data assimilation is very low.

98 In this work, we compare local wind speeds and directions measured by me-  
99 teorological stations at four different locations inside and north of the giant-  
100 dune field of the Namib sand sea to the regional predictions of the ERA5-  
101 Land climate reanalysis. Where the meteorological stations are surrounded by  
102 a relatively flat environment, we show that local measurements and regional  
103 predictions agree well. The agreement is also good in the interdune areas of  
104 the sand sea, except for some weak winds blowing at night, which exhibit an  
105 additional component aligned with the giant dune orientation, which are not  
106 predicted by the ERA5Land reanalysis (section 2). Further, we are able to link  
107 the magnitude of these differences to the circadian cycle of the atmospheric  
108 boundary layer (section 3). Finally, we draw implications for the wind dis-  
109 turbances on smaller-scale dunes (section 4), suggesting a possible origin for  
110 crossing dunes.

## 111 **2 Wind regimes across the Namib Sand Sea**

112 We measured the wind regime at four different locations in Namibia, repre-  
113 sentative of various arid environments across the Namib desert (Fig. 1, Online  
114 Resource Fig. S1). The Adamax station was located at the Adamax waterhole  
115 to the west of Etosha Pan in northern Namibia, in a sparsely vegetated area.  
116 The Huab station was near the coast on a hyper-arid flat gravel plain lying  
117 above the ephemeral Huab river. Here, 5–6 m high barchan dunes develop from  
118 the sediment blowing out of the river valley. These two stations were located  
119 in a relatively flat environments. In contrast, the North Sand Sea and South  
120 Sand Sea stations were located in the interdunes between 50–100 m high lin-

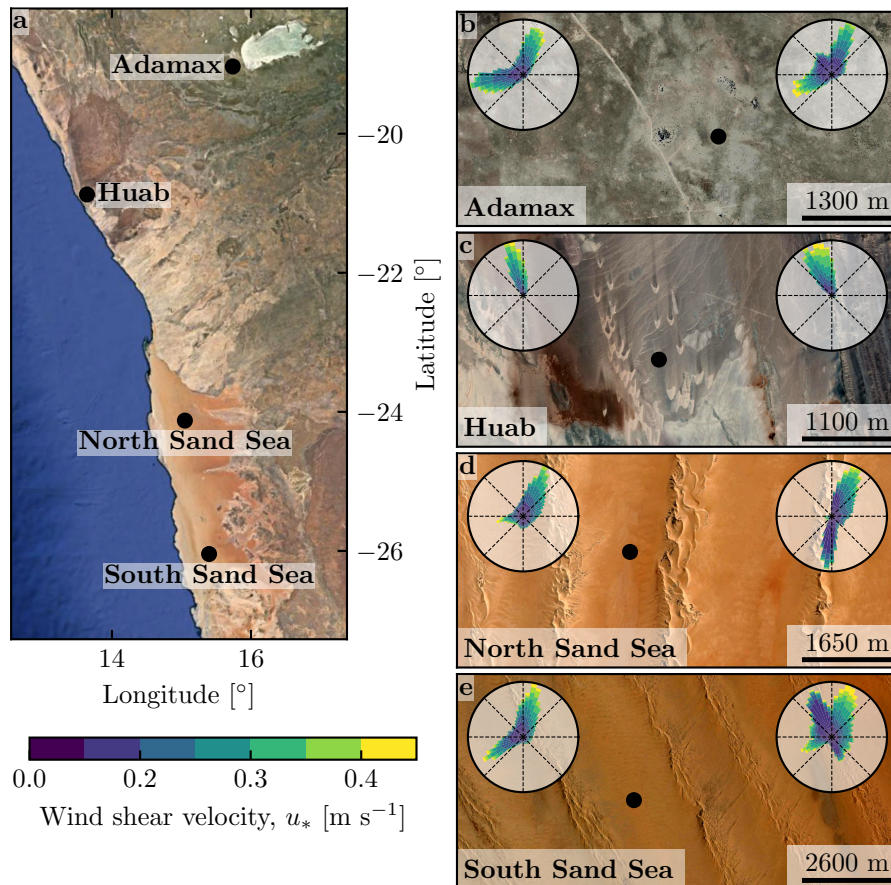


**Fig. 1** Wind data used in this study **a**: Location of the different sites in Namibia. **b–e**: Satellite images of these different environments (Google-Earth, Maxar Technologies, CNES/Airbus). In each subplot, the left and right wind roses represent the data from the ERA5-Land climate reanalysis and the local wind stations, respectively. Note that the bars show the direction towards which the wind blows. The black dots show the location of local wind stations.

ear dunes with kilometer-scale wavelengths and superimposed patterns. In this section, we describe and compare winds from local measurements and climate reanalysis predictions.

## 2.1 Wind and elevation data

At each meteorological station (Fig. 1), wind speed and direction were sampled every 10 minutes using cup anemometers and wind vanes at heights between 2 m and 3 m depending on the station. The available period of measurements at each station ranged from 1 to 5 discontinuous years distributed between 2012 and 2020 (Online Resource Fig. S2). We checked that at least one complete

130 seasonal cycle was available for each station. Regional winds were extracted  
 131 at the same locations and periods from the ERA5-Land dataset, which is a  
 132 replay at a smaller spatial resolution of ERA5, the latest climate reanalysis  
 133 from the ECMWF (Hersbach et al. 2020; Muñoz-Sabater et al. 2021). This  
 134 dataset provided hourly predictions of the 10-m wind velocity and direction  
 135 at a spatial resolution of  $0.1^\circ \times 0.1^\circ$  ( $\simeq 9$  km in Namibia).

136 To enable direct comparison, the local wind measurements were averaged  
 137 into 1-hr bins centered on the temporal scale of the ERA5-Land estimates  
 138 (Online Resource Fig. S3). As the wind velocities of both datasets were pro-  
 139 vided at different heights, we converted them into shear velocities  $u_*$  (Online  
 140 Resource section 1), characteristic of the turbulent wind profile. Wind roses  
 141 in Fig. 1(b–e) show the resulting wind data.

142 Dune properties were computed using autocorrelation on the 30-m Digital  
 143 Elevation Models (DEMs) of the shuttle radar topography mission (Farr et al.  
 144 2007). For the South Sand Sea and North Sand Sea stations, we obtain, respec-  
 145 tively, orientations of  $85^\circ$  and  $125^\circ$  with respect to the North, wavelengths of  
 146 2.6 km and 2.3 km and amplitudes (or half-heights) of 45 m and 20 m (Online  
 147 Resource Fig. S5 for more details).

## 148 2.2 Comparison of local and regional winds

149 The obtained measured and predicted wind regimes are shown in figure 1.  
 150 In the Namib, the regional wind patterns are essentially controlled by the see  
 151 breeze, resulting in strong northward components (sometimes slightly deviated  
 152 by the large scale topography) present in all regional wind roses (Lancaster  
 153 1985). These daytime winds are dominant during the period October-March  
 154 (Fig. 2f and Online Resource Fig. S6f). During April-September, an additional  
 155 easterly component can be recorded during the night, induced by the combina-  
 156 tion of katabatic winds forming in the mountains, and infrequent ‘berg’ winds,  
 157 which are responsible for the high wind velocities observed (Lancaster et al.  
 158 1984). The frequency of these easterly components decreases from inland to  
 159 the coast. As a result, bidirectional wind regimes within the Namib Sand Sea  
 160 and at the Adamax salt pan (Fig. 1b,d,e) and a unidirectional wind regime on  
 161 the coast at the outlet of the Huab River (Fig. 1c) are observed.

162 In the case of the Adamax and Huab stations, the time series of wind  
 163 speed and direction from the regional predictions quantitatively match those  
 164 corresponding to the local measurements (Fig. 2a–d) and Online Resource  
 165 Fig. S6a–d, S7). For the North Sand Sea and South Sand Sea stations within  
 166 the giant dune field, we observe that this agreement is also good, but lim-  
 167 ited to the October-March time period (Fig. 2e–h and and Online Resource  
 168 Fig. S6e–h). As a matter of fact, the measured wind roses exhibit additional  
 169 wind components aligned with the giant dune orientation, as evidenced on the  
 170 satellite images (Fig. 1c,d).

171 More precisely, during the April-September period, the local and regional  
 172 winds in the interdune match during daytime only, i.e when the southerly/southwesterly

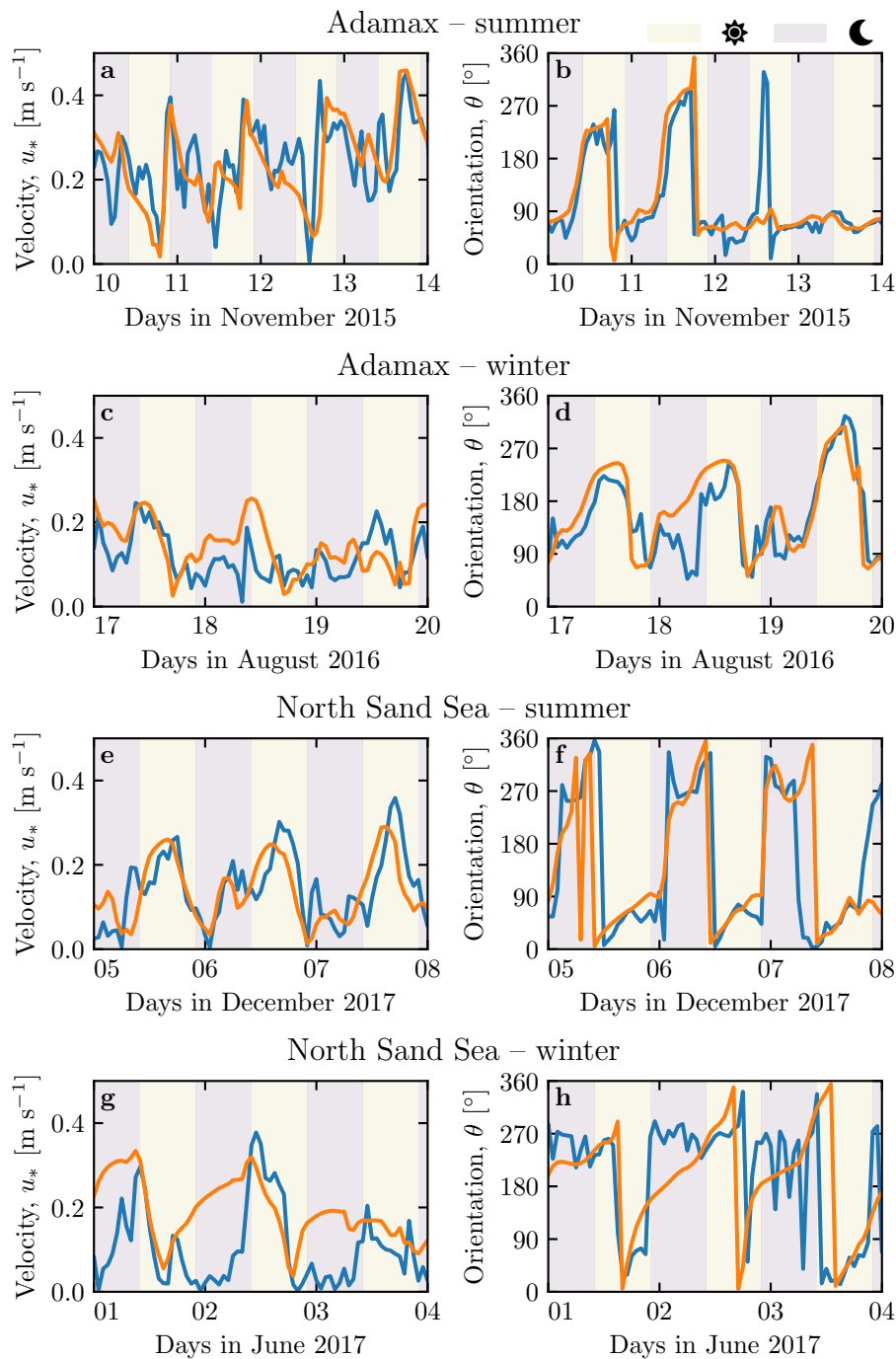


**Fig. 2** Temporal comparison between the wind data coming from the ERA5-Land climate reanalysis (orange lines) and from the local measurements (blue lines). Coloured swathes indicate day (between 1000 UTC and 2200 UTC) and night (before 1000 UTC or after 2200 UTC). **a–b:** Adamax station in summer. **b–c:** Adamax station in winter. **d–e:** North Sand Sea station in summer. **f–g:** North Sand Sea station in winter. Time series of the two other stations are shown in Online Resource Fig. S6.

173 sea breeze dominates (Figs. 2e,f and 3, Online Resource Fig. S8). In the late  
174 afternoon and during the night, when the northwesterly ‘berg’ and katabatic  
175 winds blow, measurements and predictions differ. In this case, the angular wind  
176 distribution of the local measurements exhibits two additional modes corre-  
177 sponding to reversing winds aligned with the giant dune orientation (purple  
178 frame in Fig. 3, Online Resource Figs. S8 and S9). This deviation is also as-  
179 sociated with a general attenuation of the wind strength (Online Resource  
180 Fig. S10). Remarkably, all these figures show that these wind reorientation  
181 and attenuation processes occur only at low wind velocities, typically for  
182  $u_* \lesssim 0.1 \text{ m s}^{-1}$ . For shear velocities larger than  $\simeq 0.25 \text{ m s}^{-1}$ , the wind  
183 reorientation is not apparent. Finally, for intermediate shear velocities, both  
184 situations of wind flow reoriented along the dune crest and not reoriented can  
185 be successively observed (Online Resource Fig. S9).

### 186 **3 Influence of wind speed and circadian cycle on the atmospheric 187 boundary layer**

188 The wind deflection induced by linear dunes has previously been related to the  
189 incident angle between wind direction and crest orientation, with a maximum  
190 deflection evident for incident angles between  $30^\circ$  and  $70^\circ$  (Walker et al. 2009;  
191 Hesp et al. 2015). In the data analysed here, the most deflected wind at both  
192 the North and South Sand Sea stations is seen to be where the incident angle  
193 is perpendicular to the giant dunes (Figs. 1 and 3, Online Resource Fig. S8). It  
194 therefore appears that the incident wind angle is not the dominant control on  
195 maximum wind deflection. Further, and as shown in Figure 3, winds of high  
196 and low velocities show contrasting behaviour in characteristics of deflection.  
197 This suggests a change in hydrodynamical regime between the winds. In this  
198 section, we discuss the relevant parameters associated with the dynamical  
199 mechanisms that govern the interactions between the atmospheric boundary  
200 layer flow and giant dune topographies. This analysis allows us to provide a  
201 physics-based interpretation of our measured wind data.

#### 202 **3.1 Flow over a modulated bed**

203 Taking as a reference the turbulent flow over a flat bed, the general framework  
204 of our study is understanding and describing the flow response to a bed mod-  
205 ulation (e.g. a giant dune). Without loss of generality, we can consider in this  
206 context an idealised bed elevation in the form of parallel sinusoidal ridges, with  
207 wavelength  $\lambda$  (or wavenumber  $k = 2\pi/\lambda$ ) and amplitude  $\xi_0$ , and where the ref-  
208 erence flow direction makes a given incident angle with respect to the ridge  
209 crest (Andreotti et al. 2012). Part of this response, on which we focus here,  
210 is the flow deflection by the ridges. In a simplified way, it can be understood  
211 from the Bernoulli principle (Hesp et al. 2015): as the flow approaches the  
212 ridge crest, the compression of the streamlines results in larger flow velocities,

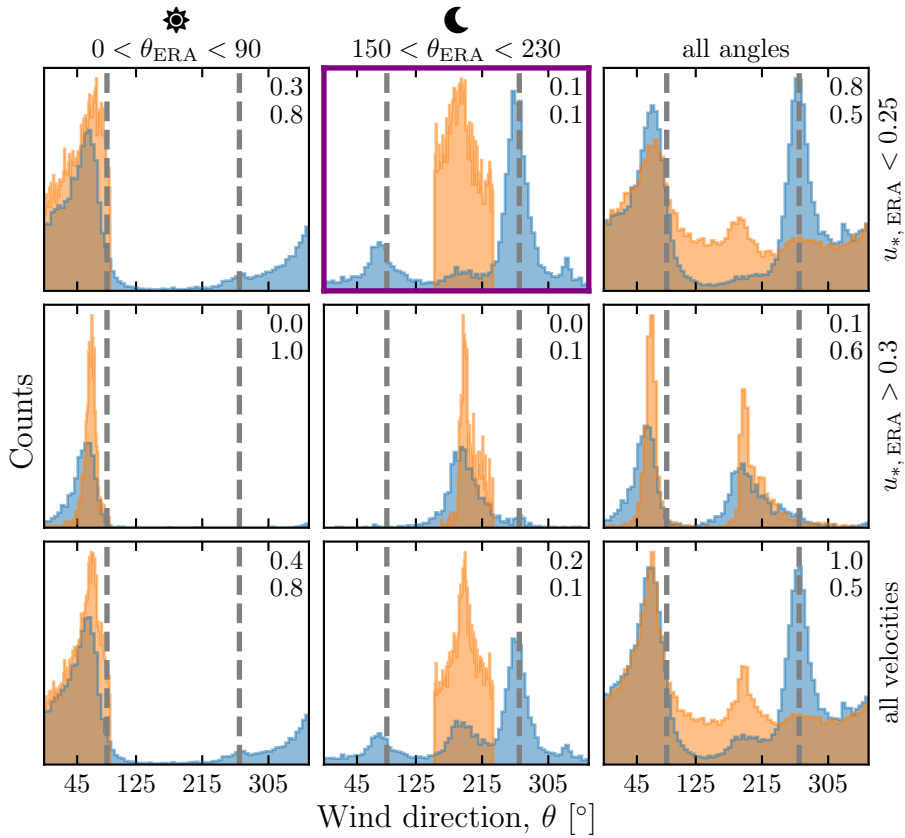


**Fig. 3** Distributions of wind direction at the North Sand Sea Station for the ERA5-Land climate reanalysis (orange) and the local measurements (blue). In each subplot, both distributions are plotted from the same time steps, selected with constraints on the wind direction (columns) and/or wind velocity (rows) of the ERA5-Land dataset. The grey vertical dashed lines indicate the dune orientation. The numbers at the top right give the percentage of time steps selected in each sub-range, as well as the percentage corresponding to the daytime (between 1000 UTC and 2200 UTC). The purple frame highlights the regime (low wind velocities, nocturnal easterly wind) in which the data from both datasets differ. A similar figure can be obtained for the North Sand Sea station (Online Resource Fig. S8).

213 and thus lower pressures (Rubin and Hunter 1987). An incident flow oblique  
 214 to the ridge is then deflected towards lower pressure zones, i.e towards the  
 215 crest. Turbulent dissipation tends to increase this effect downstream, resulting  
 216 in wind deflection along the crest in the lee side (Gadal et al. 2019).

217 Flow confinement below a capping surface, which enhances streamline com-  
 218 pression, has a strong effect on the hydrodynamic response and typically in-  
 219 creases flow deflection. This is the case for bedforms forming in open channel  
 220 flows such as rivers (Fourrière et al. 2010; Unsworth et al. 2018). This is also  
 221 relevant for aeolian dunes as they evolve in the turbulent atmospheric bound-  
 222 ary layer (ABL) capped by the stratified free atmosphere (FA) (Andreotti

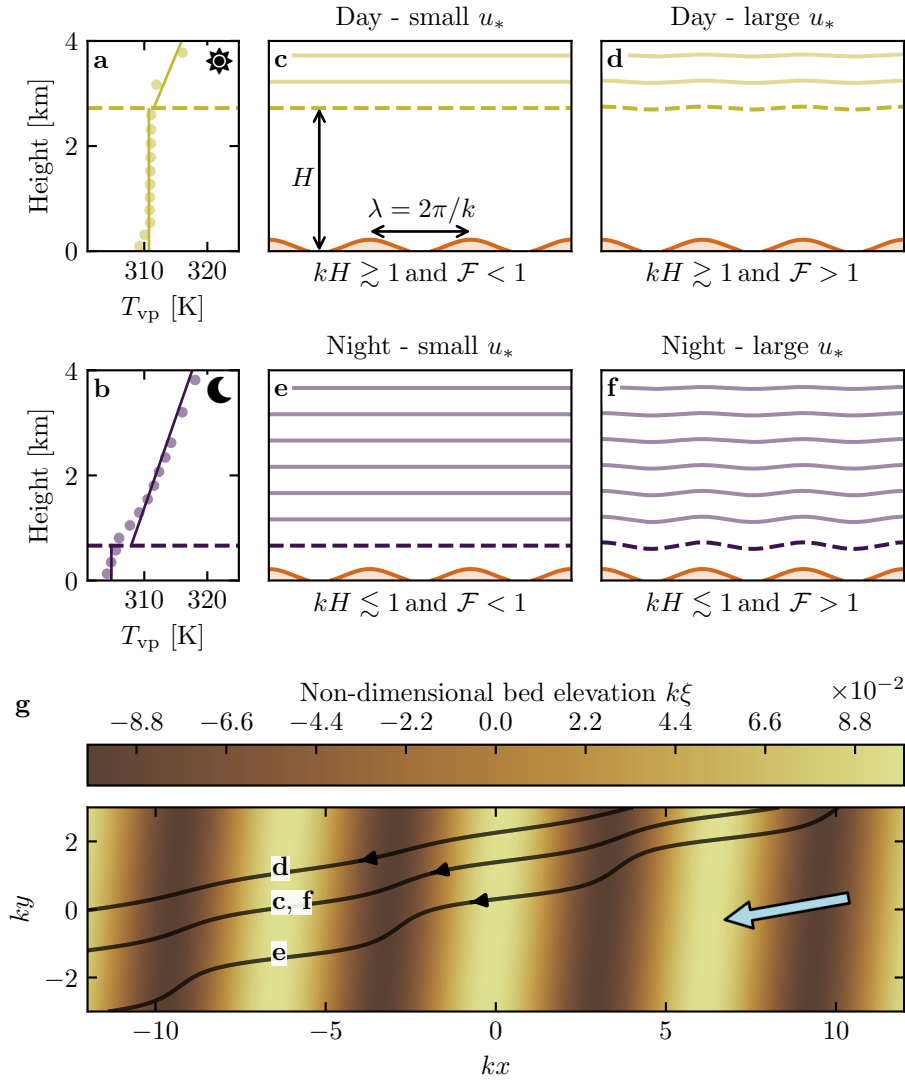


**Fig. 4** **a–b:** Vertical profiles of the virtual potential temperature at 2 different time steps (day - 03/11/2015 - 1200 UTC, night - 01/13/2013 - 0900 UTC) at the North Sand Sea station. Dots: data from the ERA5 reanalysis. Dashed lines: boundary layer height given by the ERA5 reanalysis (Online Resource section 2). Plain lines: vertical (boundary layer) and linear (free atmosphere) fits to estimate the stratification properties. **c–f:** Sketches representing the interaction between the giant dunes and the atmospheric flow for different meteorological conditions. **g:** Streamlines over a sinusoidal topography  $\xi(x, y)$  qualitatively representing the effect of low, medium and strong flow confinement, in relation to the above panels (see Appendix 1 for more details). The blue arrow indicates the undisturbed wind direction.

et al. 2009). Two main mechanisms, associated with dimensionless numbers must then be considered (Fig. 4). First, topographic obstacles typically disturb the flow over a characteristic height similar to their length. As flow confinement is characterised by a thickness  $H$ , the interaction between the dunes and the wind in the ABL is well captured by the parameter  $kH$ . The height  $H$  is directly related to the radiative fluxes at the Earth surface. It is typically on the order of a kilometre, but significantly varies with the circadian and seasonal cycles. Emerging and small dunes, with wavelengths in the range 20 to 100 m, are not affected by the confinement, corresponding to  $kH \gg 1$ . For giant dunes with kilometric wavelengths, however, their interaction with the FA is significant (Andreotti et al. 2009). This translates into a parameter  $kH$  in the range 0.02–5, depending on the moment of the day and the season. A second important mechanism is associated with the existence of a thin intermediate so-called capping layer between the ABL and the FA. It is characterised by a density jump  $\Delta\rho$ , which controls the ‘rigidity’ of this interface, i.e. how much its deformation affects streamline compression. This is usually quantified using the Froude number (Vosper 2004; Stull 2006; Sheridan and Vosper 2006; Hunt et al. 2006; Jiang 2014):

$$\mathcal{F} = \frac{U}{\sqrt{\frac{\Delta\rho}{\rho_0} g H}}, \quad (1)$$

where  $U$  is the wind velocity at the top of the ABL and  $\rho_0$  its average density. The intensity of the stratification, i.e. the amplitude of the gradient  $|\partial_z \rho|$ , also impacts its ability to deform the capping layer under the presence of an underlying obstacle, and thus affects the influence of flow confinement. This can be quantified using the internal Froude number (Vosper 2004; Stull 2006; Sheridan and Vosper 2006; Hunt et al. 2006; Jiang 2014)  $\mathcal{F}_I = kU/N$ , where  $N = \sqrt{-g\partial_z \rho/\rho_0}$  is the Brunt-Väisälä frequency (Stull 1988). Both Froude numbers have in practice the same qualitative effect on flow confinement, and we shall restrict the main discussion to  $\mathcal{F}$  only.

With this theoretical framework in mind, and in the context of the measured wind data in the North and South Sand Sea stations, the smallest wind disturbances are expected to occur during the day, when the ABL depth is the largest and comparable to the dune wavelength ( $kH \gtrsim 1$ ), which corresponds to a weak confinement situation (Fig. 4c,d). In contrast, large wind disturbances are expected to occur during the night, when the confinement is mainly induced by a shallow ABL (Fig. 4e). However, this strong confinement can be somewhat reduced in the case of strong winds, corresponding to large values of the Froude number (Fig. 4f). This is in qualitative agreement with the transition from deflected to non-deflected winds related to low and high velocities observed in our data (Sec. 2.2).

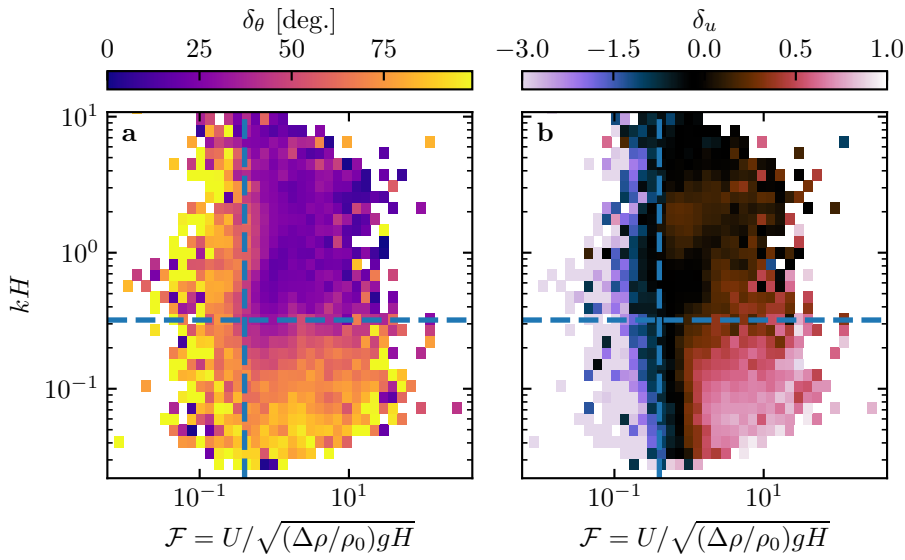


**Fig. 5** Regime diagrams of the wind deviation  $\delta_\theta$  (a) and relative attenuation/amplification  $\delta_u$  (b) in the space  $(\mathcal{F}, kH)$ , containing the data from both the North Sand Sea and South Sand Sea stations. Blue dashed lines empirically delimit the different regimes. The point density in each bin of the diagrams is shown in Online Resource Fig. S13 – 95% of the data occur in the range  $-1 < \delta_u < 1$ . Similar regime diagrams in the spaces  $(\mathcal{F}_I, kH)$  and  $(\mathcal{F}_I, \mathcal{F})$  are shown in Online Resource Fig. S14.

### 261 3.2 Data distribution in the flow regimes

262 We can go one step further and analyse how our data quantitatively spread  
 263 over the different regimes discussed above. For that purpose, one needs to  
 264 compute  $kH$  and  $\mathcal{F}$  from the time series.  $H$ ,  $U$  and the other atmospheric  
 265 parameters can be deduced from the various vertical profiles (temperature,  
 266 humidity) available in the ERA5 climate reanalysis (Online Resource section  
 267 2). We quantify the flow deflection  $\delta_\theta$  as the minimal angle between the wind  
 268 orientations comparing the local measurements and the regional predictions.  
 269 We also compute the relative velocity modulation as

$$\delta_u = \frac{u_*^{\text{ERA}} - u_*^{\text{station}}}{u_*^{\text{ERA}}}. \quad (2)$$

270 These two quantities are represented as maps in the plane  $(\mathcal{F}, kH)$  (Fig. 5a,b),  
 271 and one can clearly identify different regions in these graphs. Small wind dis-  
 272 turbances (small  $\delta_\theta$  and  $\delta_u$ ) are located in the top-right part of the diagrams,  
 273 corresponding to a regime with low-interaction as well as low-confinement ( $kH$   
 274 and  $\mathcal{F}$  large enough, Fig. 4d). Lower values of  $kH$  (stronger interaction) or of  
 275 Froude number (stronger confinement) both lead to an increase in wind dis-  
 276 turbances, both in terms of orientation and velocity. Below a crossover value  
 277  $kH \simeq 0.3$ , wind disturbance is less sensitive to the  $\mathcal{F}$ -value. This is probably

278 due to enhanced non-linear effects linked to flow modulation by the obstacle  
279 when confinement is strong. The Froude number also controls a transition from  
280 damped to amplified wind velocities in the interdune, with a crossover around  
281  $\mathcal{F} \simeq 0.4$  (Fig. 5b). Such an amplification is rather unexpected. Checking the  
282 occurrence of the corresponding data, it appears that these amplifications  
283 are associated with the southerly sea breeze, and occur dominantly during  
284 the October–March period, when the other easterly wind is not present (Online  
285 Resource Fig. S15a–b). Furthermore, they occur less frequently during  
286 the afternoon, and more frequently at the end of the day (Online Resource  
287 Fig. S15c). This effect may be linked to a change in the flow behaviour in the  
288 lee side of the obstacles but further measurements are clearly needed in order  
289 to assess the different possibilities (Baines 1995; Vosper 2004).

#### 290 **4 Discussion and conclusion**

291 The feedback of the giant dunes on the wind flow has important implications  
292 for smaller scales bedforms. As illustrated in Fig. 6, small linear dunes ( $\sim 50$  m  
293 wide) are often present in the 1–2 km interdune between giant linear dunes in  
294 the Namib Sand Sea. These smaller dunes do not exhibit the same orientation  
295 as the large ones, and are sometimes considered to be ‘crossing dunes’. Whilst  
296 differences between large and small scale dune patterns are observed ubiqui-  
297 tously, they are largely attributed to the presence of two different dune growth  
298 mechanisms, leading to two different dune patterns (orientations and/or mor-  
299 phologies) for the same wind regime (Courrech du Pont et al. 2014; Runyon  
300 et al. 2017; Lü et al. 2017; Song et al. 2019; Gadal et al. 2020; Hu et al.  
301 2021). Here, however, our arguments enable the development of differing ori-  
302 entations for the small and giant linear dunes whilst also imposing the same  
303 dune growth mechanism (elongating mode). Figure 6 shows how the orienta-  
304 tions for the small and giant dunes can be derived from the locally measured  
305 and regionally predicted winds respectively (red arrows in Fig. 6). The feed-  
306 back of the giant dunes on the wind described in this study thus provides an  
307 explanation for the existence of these small linear dunes elongating across the  
308 interdune, a dynamic which has remained unresolved to date. Further studies  
309 are of course needed to confirm this hypothesis. These crossing dunes could  
310 provide additional constraints for the inference of local winds from bedforms,  
311 similarly to what is currently performed on Mars using ripple orientations (Liu  
312 and Zimbelman 2015; Hood et al. 2021).

313 Also, this study highlights the interaction between giant dunes and the at-  
314 mospheric boundary layer. It thus supports the debated idea that the capping  
315 layer acts as a bounding surface impacting the dune dynamics, and limit-  
316 ing dune growth in particular (Andreotti et al. 2009), in contrast to an un-  
317 constrained growth ever-slower with size (Eastwood et al. 2011; Gunn et al.  
318 2021). Interestingly, this mechanism would allow for the inference of the ABL  
319 depth from the giant bedforms spacing where measurements are not feasible  
320 or available, as e.g. performed by Lorenz et al. (2010) on Titan.

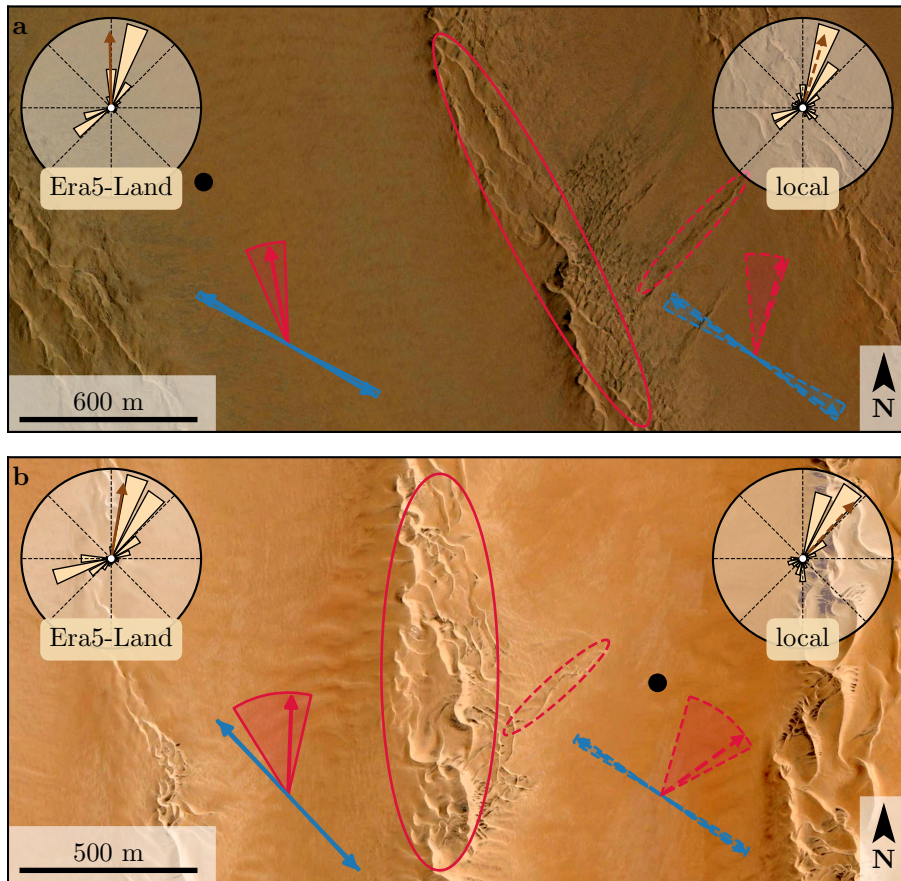


**Fig. 6** Implications for smaller scale patterns in (a) the South Sand Sea and (b) North Sand Sea. The ellipses indicate the different types of elongating dunes, at large (plain line) and small (dashed line) scales. Dune orientation are predicted using the model of Courrech du Pont et al. (2014) from the sand flux angular distributions, shown here (roses and resultant transport direction) for typical values (grain size  $180 \mu\text{m}$ , flux-up ratio of 1.6). Code for corresponding arrows: use of ERA5-Land data (plain line), use of local measurements (dashed line), prediction for the bed instability growth mechanism (blue), prediction for the elongation growth mechanism (red). Wedges show the uncertainty on the orientation calculation when parameters are varied. The black dots indicate the location of the meteorological stations with respect to the dunes. See Appendix 2 for additional details.

To sum up conditions under which the ERA5-Land reanalysis data can reliably be used to study dune morphodynamics, we summarise the comparison of local (direct measurements) and regional (climate reanalysis) wind data. In flat areas, the agreement between the two confirms the ability of the ERA5-Land climate reanalysis to predict the wind regime down to scales  $\sim 10 \text{ km}$ , i.e the model grid. When smaller scale topographies are present (giant dunes in our case), locally measured winds can significantly differ from the regionally predicted ones. This is the case when the disturbances induced by the dunes

329 interact with the lower part of the ABL vertical structure, which presents circadian variations. During the day, when the capping layer is typically high, 330 this interaction is small, and the ERA5-Land predictions are also quantitatively 331 consistent with the local data. During the night, however, the presence 332 of a shallow atmospheric boundary layer induces a strong confinement of the 333 flow, and is associated with large wind deflection by the dunes. Importantly, 334 we find that this effect can be counterbalanced for large wind velocities, which 335 are capable of deforming the capping layer, thus decreasing the influence of 336 the confinement.

337 The theoretical computation of the wind disturbances induced by sinusoidal 338 ridges under flow confinement has been performed in the linear limit 339 (Andreotti et al. 2009, 2012), i.e. when the aspect ratio of these ridges is small 340 ( $k\xi_0 \ll 1$ ). These models are able to qualitatively reproduce the observed wind 341 deflection (Appendix 1, Online Resource Figs. S14 and S16), and thus provide 342 the physical support for the interpretation we propose here based on hydrodynamic 343 regimes. However, these models cannot quantitatively predict the magnitude 344 of these observations, probably due to the presence of expected non-linearities 345 in high confinement situations linked to strong flow modulations. Besides, 346 these linear calculations only predict wind attenuation in the interdune, in contrast 347 with the observed enhanced velocities associated with particular evening winds from 348 the South during the period October-March (Online Resource Fig. S15). Some other 349 models predict different spatial flow structures in response to a modulated topography, such 350 as lee waves and rotors (Baines 1995; Vosper 2004). Of course they cannot be 351 observed by our measurements located at a single point in the interdune. Data at different 352 places along and across the ridges are needed to investigate and possibly map such 353 flow structures, and for further comparisons with the models.

355 **Acknowledgements** We would like to acknowledge the contributors of the following open-source python libraries, Matplotlib (Hunter 2007), Numpy (Harris et al. 2020) and Scipy (Virtanen et al. 2020), which provide an incredibly efficient ecosystem allowing scientific research in Python.

356 ERA5 and ERA5-Land datasets are publicly available at the Copernicus Climate Change 357 Service (C3S) Climate Data Store. The locally measured wind data can be found at [upload on public data repository](#). The digital elevation models from the Shuttle Radar Topography Mission are publicly available from Nasa servers, and can be downloaded at <https://dwtkns.com/srtm30m/>. Fully documented codes used to analyse this study are 358 available at <https://github.com/Cgadal/GiantDunes> (will be made public upon acceptance 359 of this manuscript for publication).

360 [citing all relevant grants ...] [TOAD](#)

### 361 **Appendix 1: Linear theory of wind response to topographic perturbation**

362 Following the work of Fourrière et al. (2010), Andreotti et al. (2012) and 363 Andreotti et al. (2009), we briefly describe in this appendix the framework 364 for the linear response of a turbulent flow to a topographic perturbation of

<sup>373</sup> small aspect ratio. As a general bed elevation can be decomposed into Fourier  
<sup>374</sup> modes, we focus here on a sinusoidal topography:

$$\xi = \xi_0 \cos [k (\cos(\alpha)y - \sin(\alpha)x)], \quad (3)$$

<sup>375</sup> which is also a good approximation for the giant dunes observed in the North  
<sup>376</sup> Sand Sea and South Sand Sea Station (Fig. 1 and Online Resource Fig. S5).  
<sup>377</sup> Here,  $x$  and  $y$  are the streamwise and spanwise coordinates,  $k = 2\pi/\lambda$  the  
<sup>378</sup> wavenumber of the sinusoidal perturbation,  $\alpha$  its crest orientation with respect  
<sup>379</sup> to the  $x$ -direction (anticlockwise) and  $\xi_0$  its amplitude. The two components  
<sup>380</sup> of the basal shear stress  $\tau = \rho_0 u_* \mathbf{u}_*$ , constant in the flat bottom reference  
<sup>381</sup> case, can then be generically written as:

$$\tau_x = \tau_0 \left( 1 + k\xi_0 \sqrt{\mathcal{A}_x^2 + \mathcal{B}_x^2} \cos [k (\cos(\alpha)y - \sin(\alpha)x) + \phi_x] \right), \quad (4)$$

$$\tau_y = \tau_0 k\xi_0 \sqrt{\mathcal{A}_y^2 + \mathcal{B}_y^2} \cos [k (\cos(\alpha)y - \sin(\alpha)x) + \phi_y], \quad (5)$$

<sup>382</sup> where  $\tau_0$  is the reference basal shear stress on a flat bed. We have defined  
<sup>383</sup> the phase  $\phi_{x,y} = \tan^{-1}(\mathcal{B}_{x,y}/\mathcal{A}_{x,y})$  from the in-phase and in-quadrature hy-  
<sup>384</sup> drodynamical coefficients  $\mathcal{A}_{x,y}$  and  $\mathcal{B}_{x,y}$ . They are functions of  $k$  and of the  
<sup>385</sup> flow conditions, i.e the bottom roughness, the vertical flow structure and the  
<sup>386</sup> incident flow direction, and the theoretical framework developed in the above  
<sup>387</sup> cited papers proposes methods to compute them in the linear regime.

<sup>388</sup> Following Andreotti et al. (2012), the effect of the incident wind direction  
<sup>389</sup> can be approximated by the following expressions:

$$\mathcal{A}_x = \mathcal{A}_0 \sin^2 \alpha, \quad (6)$$

$$\mathcal{B}_x = \mathcal{B}_0 \sin^2 \alpha, \quad (7)$$

$$\mathcal{A}_y = -\frac{1}{2} \mathcal{A}_0 \cos \alpha \sin \alpha, \quad (8)$$

$$\mathcal{B}_y = -\frac{1}{2} \mathcal{B}_0 \cos \alpha \sin \alpha, \quad (9)$$

<sup>390</sup> where  $\mathcal{A}_0$  and  $\mathcal{B}_0$  are now two coefficients independent of the dune orienta-  
<sup>391</sup> tion  $\alpha$ , corresponding to the transverse case ( $\alpha = 90^\circ$ ). For a fully turbulent  
<sup>392</sup> boundary layer capped by a stratified atmosphere, these coefficients depend  
<sup>393</sup> on  $kH$ ,  $kz_0$ ,  $\mathcal{F}$  and  $\mathcal{F}_I$  (Andreotti et al. 2009). In this study, we assume a con-  
<sup>394</sup> stant hydrodynamic roughness  $z_0 \simeq 1$  mm (Online Resource section 1). For  
<sup>395</sup> the considered giant dunes, this leads to  $kz_0 \simeq 2 \cdot 10^{-6}$ , as their wavelength  
<sup>396</sup> is  $\lambda \simeq 2.4$  km (or  $k \simeq 2 \cdot 10^{-3}$  m $^{-1}$ ). Values of  $z_0$  extracted from field data  
<sup>397</sup> indeed typically fall between 0.1 mm and 10 mm (Sherman and Farrell 2008;  
<sup>398</sup> Field and Pelletier 2018). Importantly,  $\mathcal{A}_0$  and  $\mathcal{B}_0$  do not vary much in the  
<sup>399</sup> corresponding range of  $kz_0$  (Fourrière et al. 2010), and the results presented  
<sup>400</sup> here are robust with respect to this choice.

<sup>401</sup> With capping layer height and Froude numbers computed from the ERA5-  
<sup>402</sup> Land time series, the corresponding  $\mathcal{A}_0$  and  $\mathcal{B}_0$  can be deduced, allowing to  
<sup>403</sup> produce maps as displayed in Online Resource Fig. S16. Interestingly, it shows

similar regimes as in the diagrams of Fig. 5 and Online Resource Fig. S14a,b, supporting the physics picture. However, the matching remains qualitative only. As a matter of fact, the linearity assumption of the theoretical framework requires  $(|\tau| - \tau_0)/\tau_0 \ll 1$ , which translates into  $k\xi\sqrt{\mathcal{A}_0^2 + \mathcal{B}_0^2} \ll 1$ . In our case, the giant dune morphology gives  $k\xi_0 \simeq 0.1$ , which means that one quits the regime of validity of the linear theory when the coefficient modulus  $\sqrt{\mathcal{A}_0^2 + \mathcal{B}_0^2}$  becomes larger than a few units. In accordance with the theoretical expectations, these coefficients present values on the order of unity ( $\mathcal{A}_0 \simeq 3$  and  $\mathcal{B}_0 \simeq 1$ ) in unconfined situations (Claudin et al. 2013; Lü et al. 2021). In contrast and as illustrated in Online Resource Fig. S16a,b, larger values are predicted in case of strong confinement, which does not allow us to proceed to further quantitative comparison with the data.

Finally, the linear model is also able to reproduce the enhancement of the flow deflection over the sinusoidal ridges when  $\sqrt{\mathcal{A}_0^2 + \mathcal{B}_0^2}$  is increased (Online Resource Fig. S16). Here, using  $k\xi_0 \simeq 0.1$  to be representative of the amplitude of the giant dunes at the North Sand Sea station, the coefficient modulus is bounded to 10.

## Appendix 2: Sediment transport and dune morphodynamics

We summarise in this appendix the sediment transport and dune morphodynamics theoretical framework leading to the prediction of sand fluxes and dune orientations from wind data.

*Sediment transport* — The prediction of sand fluxes from wind data has been a long standing issue in aeolian geomorphological studies (Fryberger and Dean 1979; Pearce and Walker 2005; Sherman and Li 2012; Shen et al. 2019). Based on laboratory studies in wind tunnels (Rasmussen et al. 1996; Iversen and Rasmussen 1999; Creyssels et al. 2009; Ho et al. 2011), as well as physical considerations (Ungar and Haff 1987; Andreotti 2004; Durán et al. 2011; Pähzt and Durán 2020), it has been shown that the steady saturated saltation flux over a flat sand bed depends linearly on the shear stress:

$$\frac{q_{\text{sat}}}{Q} = \Omega \sqrt{\Theta_{\text{th}}} (\Theta - \Theta_{\text{th}}), \quad (10)$$

where  $\Omega$  is a proportionality constant,  $Q = d\sqrt{(\rho_s - \rho_0)gd/\rho_0}$  is a characteristic flux,  $\Theta = \rho_0 u_*^2 / (\rho_s - \rho_0)gd$  the Shields number, and  $\Theta_{\text{th}}$  its threshold value below which saltation vanishes.  $\rho_s = 2.6 \text{ g cm}^{-3}$  and  $d = 180 \mu\text{m}$  are the grain density and diameter, and  $g$  is the gravitational acceleration. The shear velocity, and consequently the Shields number as well as the sediment flux, are time dependent.

Recently, Pähzt and Durán (2020) suggested an additional quadratic term in Shields to account for grain-grain interactions within the transport layer at strong wind velocities:

$$\frac{q_{\text{sat}, t}}{Q} = \frac{2\sqrt{\Theta_{\text{th}}}}{\kappa\mu} (\Theta - \Theta_{\text{th}}) \left( 1 + \frac{C_M}{\mu} [\Theta - \Theta_{\text{th}}] \right), \quad (11)$$

where  $\kappa = 0.4$  is the von Kármán constant,  $C_M \simeq 1.7$  a constant and  $\mu \simeq 0.6$  is a friction coefficient, taken to be the avalanche slope of the granular material. The fit of this law to the experimental data of Creyssels et al. (2009) and Ho et al. (2011) gives  $\Theta_{\text{th}} = 0.0035$ . The fit of Eq. 10 on these same data similarly gives  $\Omega \simeq 8$  and  $\Theta_{\text{th}} = 0.005$ . The sand flux angular distributions and the dune orientations in Fig. 6 are calculated using this law (11). We have checked that using the ordinary linear relationship (10) instead does not change the predicted dune orientations by more than a few degrees.

*Dune orientations* — Dune orientations are predicted with the dimensional model of Courrech du Pont et al. (2014), from the sand flux time series computed with the above transport law. Two orientations are possible depending on the mechanism dominating the dune growth: elongation or bed instability. The orientation  $\alpha$  corresponding the bed instability is then the one that maximises the following growth rate (Rubin and Hunter 1987):

$$\sigma \propto \frac{1}{H_d W_d T} \int_0^T q_{\text{crest}} |\sin(\theta - \alpha)| dt, \quad (12)$$

where  $\theta$  is the wind orientation measured with respect to the same reference as  $\alpha$ , and  $H_d$  and  $W_d$  are dimensional constants respectively representing the dune height and width. The integral runs over a time  $T$ , which must be representative of the characteristic period of the wind regime. The flux at the crest is expressed as:

$$q_{\text{crest}} = q_{\text{sat}} [1 + \gamma |\sin(\theta - \alpha)|], \quad (13)$$

where the flux-up ratio  $\gamma$  has been calibrated to 1.6 using field studies, underwater laboratory experiments and numerical simulations. Predictions of the linear analysis of Gadal et al. (2019) and Delorme et al. (2020) give similar results.

Similarly, the dune orientation corresponding to the elongation mechanism is the one that verifies:

$$\tan(\alpha) = \frac{\langle q_{\text{crest}}(\alpha) e_\theta \rangle \cdot e_{WE}}{\langle q_{\text{crest}}(\alpha) e_\theta \rangle \cdot e_{SN}}, \quad (14)$$

where  $\langle \cdot \rangle$  denotes a vectorial time average. The unitary vectors  $e_{WE}$ ,  $e_{SN}$  and  $e_\theta$  are in the West-East, South-North and wind directions, respectively.

The resulting computed dune orientations, blue and red arrows in Fig. 6, then depend on a certain number of parameters (grain properties, flux-up ratio, etc.), for which we take typical values for aeolian sandy deserts. Due to the lack of measurements in the studied places, some uncertainties can be expected. We therefore run a sensitivity test by calculating the dune orientations for grain diameters ranging from  $100 \mu\text{m}$  to  $400 \mu\text{m}$  and for a speed-up ratio between 0.1 and 10 (wedges in Fig. 6).

---

**476 References**

- 477 Andreotti B (2004) A two-species model of aeolian sand transport. *J Fluid  
478 Mech* 510:47–70
- 479 Andreotti B, Fourrière A, Ould-Kaddour F, Murray B, Claudin P (2009) Gi-  
480 ant aeolian dune size determined by the average depth of the atmospheric  
481 boundary layer. *Nature* 457:1120–1123
- 482 Andreotti B, Claudin P, Devauchelle O, Durán O, Fourrière A (2012) Bedforms  
483 in a turbulent stream: ripples, chevrons and antidunes. *J Fluid Mech* 690:94–  
484 128
- 485 Ashkenazy Y, Yizhaq H, Tsoar H (2012) Sand dune mobility under climate  
486 change in the kalahari and australian deserts. *Climatic Change* 112:901–923
- 487 Baddock M, Livingstone I, Wiggs G (2007) The geomorphological significance  
488 of airflow patterns in transverse dune interdunes. *Geomorphology* 87:322–  
489 336
- 490 Baines PG (1995) Topographic effects in stratified flows. Cambridge university  
491 press
- 492 Bauer BO, Sherman DJ, Wolcott JF (1992) Sources of uncertainty in shear  
493 stress and roughness length estimates derived from velocity profiles. *Prof  
494 Geogr* 44:453–464
- 495 Belcher S, JCR H (1998) Turbulent flow over hills and waves. *Annu Rev Fluid  
496 Mech* 30:507–538
- 497 Blumberg DG, Greeley R (1996) A comparison of general circulation model  
498 predictions to sand drift and dune orientations. *J Clim* 9:3248–3259
- 499 Bristow NR, Best J, Wiggs GFS, Nield JM, Baddock MC, Delorme P, Chris-  
500 tensen KT (2022) Topographic perturbation of turbulent boundary layers  
501 by low-angle, early-stage aeolian dunes. *Earth Surface Processes and Land-  
502 forms* n/a(n/a), DOI <https://doi.org/10.1002/esp.5326>
- 503 Brown S, Nickling WG, Gillies JA (2008) A wind tunnel examination of shear  
504 stress partitioning for an assortment of surface roughness distributions. *J  
505 Geophys Res* 113:F02S06
- 506 Charru F, Andreotti B, Claudin P (2013) Sand ripples and dunes. *Annu Rev  
507 Fluid Mech* 45:469–493
- 508 Claudin P, Wiggs G, Andreotti B (2013) Field evidence for the upwind velocity  
509 shift at the crest of low dunes. *Boundary-layer Meteorol* 148:195–206
- 510 Claudin P, Durán O, Andreotti B (2017) Dissolution instability and roughen-  
511 ing transition. *J Fluid Mech* 832:R2
- 512 Claudin P, Louge M, Andreotti B (2021) Basal pressure variations induced by  
513 a turbulent flow over a wavy surface. *Front Phys* 9:682,564
- 514 Courrech du Pont S (2015) Dune morphodynamics. *C R Physique* 16:118–138
- 515 Courrech du Pont S, Narteau C, Gao X (2014) Two modes for dune orientation.  
516 *Geology* 42:743–746
- 517 Creyssels M, Dupont P, El Mohtar AO, Valance A, Cantat I, Jenkins JT, Pasini  
518 JM, Rasmussen KR (2009) Saltating particles in a turbulent boundary layer:  
519 experiment and theory. *J Fluid Mech* 625:47–74

- 520 Dee DP, Uppala SM, Simmons AJ, Berrisford P, Poli P, Kobayashi S, Andrae  
521 U, Balmaseda M, Balsamo G, Bauer dP, et al. (2011) The era-interim re-  
522 analysis: Configuration and performance of the data assimilation system. *Q*  
523 *J R Meteorol Soc* 137:553–597
- 524 Delorme P, Wiggs G, Baddock M, Claudin P, Nield J, Valdez A (2020) Dune  
525 initiation in a bimodal wind regime. *J Geophys Res* 125:e2020JF005,757
- 526 Durán O, Claudin P, Andreotti B (2011) On aeolian transport: Grain-scale  
527 interactions, dynamical mechanisms and scaling laws. *Aeolian Res* 3:243–  
528 270
- 529 Durran DR (1990) Mountain waves and downslope winds. In: *Atmospheric*  
530 *processes over complex terrain*, Springer, pp 59–81
- 531 Eastwood E, Nield J, Baas A, Kocurek G (2011) Modelling controls on aeolian  
532 dune-field pattern evolution. *Sedimentology* 58:1391–1406
- 533 Farr TG, Rosen PA, Caro E, Crippen R, Duren R, Hensley S, Kobrick M,  
534 Paller M, Rodriguez E, Roth L, et al. (2007) The shuttle radar topography  
535 mission. *Rev Geophys* 45
- 536 Fernando H, Mann J, Palma J, Lundquist JK, Barthelmie RJ, Belo-Pereira M,  
537 Brown W, Chow F, Gerz T, Hocut C, et al. (2019) The perdigão: Peering  
538 into microscale details of mountain winds. *Bull Amer Meteor Soc* 100:799–  
539 819
- 540 Field JP, Pelletier JD (2018) Controls on the aerodynamic roughness length  
541 and the grain-size dependence of aeolian sediment transport. *Earth Surf*  
542 *Process Landforms* 43:2616–2626
- 543 Finnigan J, Raupach M, Bradley E, Aldis G (1990) A wind tunnel study  
544 of turbulent flow over a two-dimensional ridge. *Boundary-layer Meteorol*  
545 50:277–317
- 546 Finnigan J, Ayotte K, Harman I, Katul G, Oldroyd H, Patton E, Poggi D,  
547 Ross A, Taylor P (2020) Boundary-layer flow over complex topography.  
548 *Boundary-layer Meteorol* 177:247–313
- 549 Flack K, Schultz M (2010) Review of hydraulic roughness scales in the fully  
550 rough regime. *J Fluids Eng* 132:041,203
- 551 Fourrière A, Claudin P, Andreotti B (2010) Bedforms in a turbulent stream:  
552 formation of ripples by primary linear instability and of dunes by nonlinear  
553 pattern coarsening. *J Fluid Mech* 649:287–328
- 554 Frederick KA, Hanratty TJ (1988) Velocity measurements for a turbulent non-  
555 separated flow over solid waves. *Exp Fluids* 6:477–486
- 556 Fryberger SG, Dean G (1979) Dune forms and wind regime. A study of global  
557 sand seas 1052:137–169
- 558 Gadal C, Narteau C, Courrech Du Pont S, Rozier O, Claudin P (2019) Incip-  
559 ient bedforms in a bidirectional wind regime. *J Fluid Mech* 862:490–516
- 560 Gadal C, Narteau C, Courrech du Pont S, Rozier O, Claudin P (2020) Peri-  
561 odicity in fields of elongating dunes. *Geology* 48:343–347
- 562 Gong W, Ibbetson A (1989) A wind tunnel study of turbulent flow over model  
563 hills. *Boundary-layer Meteorol* 49:113–148
- 564 Gong W, Taylor P, Dörnbrack A (1996) Turbulent boundary-layer flow over  
565 fixed aerodynamically rough two-dimensional sinusoidal waves. *J Fluid Mech*

- 566 312:1–37
- 567 Gunn A, Wanker M, Lancaster N, Edmonds D, Ewing R, Jerolmack  
568 D (2021) Circadian rhythm of dune-field activity. *Geophys Res Lett*  
569 48:e2020GL090,924
- 570 Harris CR, Millman KJ, van der Walt SJ, Gommers R, Virtanen P, Cournapeau D, Wieser E, Taylor J, Berg S, Smith NJ, et al. (2020) Array program-  
571 ming with numpy. *Nature* 585:357–362
- 572 Hersbach H, Bell B, Berrisford P, Hirahara S, Horányi A, Muñoz-Sabater J,  
573 Nicolas J, Peubey C, Radu R, Schepers D, et al. (2020) The era5 global  
574 reanalysis. *Q J R Meteorol Soc* 146:1999–2049
- 575 Hesp PA, Smyth TAG, Nielsen P, Walker IJ, Bauer BO, Davidson-Arnott R  
576 (2015) Flow deflection over a foredune. *Geomorphology* 230:64–74
- 577 Ho TD, Valance A, Dupont P, Ould El Moctar A, Tuan Duc H, Valance A,  
578 Dupont P, Ould El Moctar A (2011) Scaling laws in aeolian sand transport.  
579 *Phys Rev Lett* 106:4–7
- 580 Hood DR, Ewing RC, Roback KP, Runyon K, Avouac JP, McEnroe M (2021)  
581 Inferring airflow across martian dunes from ripple patterns and dynamics.  
582 *Front Earth Sci* 9:702,828
- 583 Howard AD (1977) Effect of slope on the threshold of motion and its applica-  
584 tion to orientation of wind ripples. *Geol Soc Am Bull* 88:853–856
- 585 Hu Z, Gao X, Lei J, Zhou N (2021) Geomorphology of aeolian dunes in the  
586 western sahara desert. *Geomorphology* 392:107,916
- 587 Hunt J, Leibovich S, Richards K (1988) Turbulent shear flows over low hills.  
588 *Q J R Meteorol Soc* 114:1435–1470
- 589 Hunt JCR, Vilenski GG, Johnson ER (2006) Stratified separated flow around  
590 a mountain with an inversion layer below the mountain top. *J Fluid Mech*  
591 556:105–119
- 592 Hunter JD (2007) Matplotlib: A 2d graphics environment. *Computing in sci-  
593 ence & engineering* 9:90–95
- 594 Iversen JD, Rasmussen KR (1999) The effect of wind speed and bed slope on  
595 sand transport. *Sedimentology* 46:723–731
- 596 Jackson PS, Hunt JCR (1975) Turbulent wind flow over a low hill. *Q J R  
597 Meteorol Soc* 101:929–955
- 598 Jiang Q (2014) Applicability of reduced-gravity shallow-water theory to atmo-  
599 pheric flow over topography. *J Atmos Sci* 71:1460–1479
- 600 Jolivet M, Braucher R, Dovchintseren D, Hocquet S, Schmitt J, ASTER Team  
601 (2021) Erosion around a large-scale topographic high in a semi-arid sedimen-  
602 tary basin: Interactions between fluvial erosion, aeolian erosion and aeolian  
603 transport. *Geomorphology* 386:107,747
- 604 Kim HG, Patel VC, Lee CM (2000) Numerical simulation of wind flow  
605 over hilly terrain. *Journal of wind engineering and industrial aerodynamics*  
606 87:45–60
- 607 Lancaster J, Lancaster N, Seely M (1984) Climate of the central namib desert.  
608 Madoqua 1984:5–61
- 609 Lancaster N (1985) Winds and sand movements in the namib sand sea. *Earth  
610 Surf Process Landforms* 10:607–619

- 612 Lewis HW, Mobbs SD, Lehning M (2008) Observations of cross-ridge flows  
613 across steep terrain. *Q J R Meteorol Soc* 134:801–816
- 614 Liu ZYC, Zimbelman JR (2015) Recent near-surface wind directions inferred  
615 from mapping sand ripples on martian dunes. *Icarus* 261:169–181
- 616 Livingstone I, Warren A (2019) Aeolian geomorphology: an new introduction.  
617 Wiley
- 618 Livingstone I, Bristow C, Bryant RG, Bullard J, White K, Wiggs GFS, Baas  
619 ACW, Bateman MD, Thomas DSG (2010) The namib sand sea digital  
620 database of aeolian dunes and key forcing variables. *Aeolian Res* 2:93–104
- 621 Lorenz R, Claudin P, Andreotti B, Radabaugh J, Tokano T (2010) A 3 km  
622 atmospheric boundary layer on titan indicated by dune spacing and huygens  
623 data. *Icarus* 205:719–721
- 624 Lü P, Narteau C, Dong Z, Rozier O, Du Pont SC (2017) Unravelling raked  
625 linear dunes to explain the coexistence of bedforms in complex dunefields.  
626 *Nature comm* 8:1–9
- 627 Lü P, Narteau C, Dong Z, Claudin P, Rodriguez S, An Z, Fernandez-Cascales  
628 L, Gadal C, Courrech du Pont S (2021) Direct validation of dune instability  
629 theory. *Proc Natl Acad Sci USA* 118
- 630 Mason P, Sykes R (1979) Flow over an isolated hill of moderate slope. *Q J R  
631 Meteorol Soc* 105:383–395
- 632 Muñoz-Sabater J, Dutra E, Agustí-Panareda A, Albergel C, Arduini G, Bal-  
633 samo G, Boussetta S, Choulga M, Harrigan S, Hersbach H, et al. (2021)  
634 Era5-land: A state-of-the-art global reanalysis dataset for land applications.  
635 *Earth Syst Sci Data* 13:4349–4383
- 636 Nield JM, King J, Wiggs GFS, Leyland J, Bryant RG, Chiverrell RC, Darby  
637 SE, Eckhardt FD, Thomas DSG, Vircavs LH, Washington R (2014) Esti-  
638 mating aerodynamic roughness over complex surface terrain. *J Geophys Res*  
639 118:12,948–12,961
- 640 Pähzt T, Durán O (2020) Unification of aeolian and fluvial sediment transport  
641 rate from granular physics. *Phys Rev Lett* 124:168,001
- 642 Pearce KI, Walker IJ (2005) Frequency and magnitude biases in the 'Fryberger'  
643 model, with implications for characterizing geomorphically effective winds.  
644 *Geomorphology* 68:39–55
- 645 Pelletier JD, Field JP (2016) Predicting the roughness length of turbulent flows  
646 over landscapes with multi-scale microtopography. *Earth Surface Dynamics*  
647 4:391–405
- 648 Poggi D, Katul G, Albertson J, Ridolfi L (2007) An experimental investigation  
649 of turbulent flows over a hilly surface. *Phys Fluids* 19:036,601
- 650 Rasmussen KR, Iversen JD, Rautaheimo P (1996) Saltation and wind flow  
651 interaction in a variable slope wind tunnel. *Geomorphology* 17:19–28
- 652 Raupach M (1992) Drag and drag partition on rough surfaces. *Boundary-layer  
653 Meteorol* 60:375–395
- 654 Rubin DM, Hunter RE (1987) Bedform alignment in directionally varying  
655 flows. *Science* 237:276–278
- 656 Runyon K, Bridges N, Ayoub F, Newman C, Quade J (2017) An integrated  
657 model for dune morphology and sand fluxes on mars. *Earth Planet Sci Lett*

- 658 457:204–212
- 659 Seidel DJ, Zhang Y, Beljaars A, Golaz JC, Jacobson AR, Medeiros B (2012)  
660 Climatology of the planetary boundary layer over the continental united  
661 states and europe. *J Geophys Research* 117:D17,106
- 662 Shao Y (2008) Physics and modelling of wind erosion, vol 37. Springer Science  
663 & Business Media
- 664 Shen Y, Zhang C, Huang X, Wang X, Cen S (2019) The effect of wind speed  
665 averaging time on sand transport estimates. *Catena* 175:286–293
- 666 Sheridan PF, Vosper SB (2006) A flow regime diagram for forecasting lee  
667 waves, rotors and downslope winds. *Meteorological Applications* 13:179–195
- 668 Sherman D, Farrell E (2008) Aerodynamic roughness lengths over movable  
669 beds: Comparison of wind tunnel and field data. *J Geophys Res* 113:1–10
- 670 Sherman DJ, Li B (2012) Predicting aeolian sand transport rates: A reevalu-  
671 ation of models. *Aeolian Res* 3:371–378
- 672 Smith AB, Jackson DWT, Cooper JAG (2017) Three-dimensional airflow and  
673 sediment transport patterns over barchan dunes. *Geomorphology* 278:28–42
- 674 Song Q, Gao X, Lei J, Li S (2019) Spatial distribution of sand dunes and their  
675 relationship with fluvial systems on the southern margin of the taklimakan  
676 desert, china. *Geomatics, Natural Hazards and Risk* 10:2408–2428
- 677 Spalding DB (1961) A single formula for the law of the wall. *J Applied Mech*  
678 28:455–458
- 679 Stull R (2006) 9 - the atmospheric boundary layer. In: Wallace JM, Hobbs PV  
680 (eds) *Atmospheric Science* (Second Edition), second edition edn, Academic  
681 Press, San Diego, pp 375–417
- 682 Stull RB (1988) An introduction to boundary layer meteorology, vol 13.  
683 Springer Science & Business Media
- 684 Sullivan PP, McWilliams JC (2010) Dynamics of winds and currents coupled  
685 to surface waves. *Annu Rev Fluid Mech* 42:19–42
- 686 Sykes RI (1980) An asymptotic theory of incompressible turbulent boundary-  
687 layer flow over a small hump. *J Fluid Mech* 101:647–670
- 688 Taylor P, Teunissen H (1987) The Askervein hill project: overview and back-  
689 ground data. *Boundary-layer Meteorol* 39:15–39
- 690 Taylor P, Mason P, Bradley E (1987) Boundary-layer flow over low hills.  
691 *Boundary-layer Meteorol* 39:107–132
- 692 Ungar JE, Haff PK (1987) Steady state saltation in air. *Sedimentology* 34:289–  
693 299
- 694 Unsworth C, Parsons D, Hardy R, Reesink A, Best J, Ashworth P, Keevil G  
695 (2018) The impact of nonequilibrium flow on the structure of turbulence  
696 over river dunes. *Water Resour Res* 54:6566–6584
- 697 Uppala SM, Källberg P, Simmons AJ, Andrae U, Bechtold VDC, Fiorino M,  
698 Gibson J, Haseler J, Hernandez A, Kelly G, et al. (2005) The era-40 re-  
699 analysis. *Q J R Meteorol Soc* 131:2961–3012
- 700 Valance A, Rasmussen K, Ould El Moctar A, Dupont P (2015) The physics  
701 of aeolian sand transport. *C R Physique* 16:1–13
- 702 Virtanen P, Gommers R, Oliphant TE, Haberland M, Reddy T, Cournapeau  
703 D, Burovski E, Peterson P, Weckesser W, Bright J, et al. (2020) Scipy 1.0:

- 704 fundamental algorithms for scientific computing in python. *Nature methods*  
705 17:261–272
- 706 Vogelezang D, Holtslag A (1996) Evaluation and model impacts of alternative  
707 boundary-layer height formulations. *Boundary-layer Meteorol* 81:245–269
- 708 Vosper SB (2004) Inversion effects on mountain lee waves. *Q J R Meteorol Soc*  
709 130:1723–1748
- 710 Walker I, Davidson-Arnott R, Bauer B, Hesp P, Delgado-Fernandez I, Oller-  
711 head J, Smyth T (2017) Scale-dependent perspectives on the geomorphology  
712 and evolution of beach-dune systems. *Earth-Science Rev* 171:220–253
- 713 Walker IJ, Hesp PA, Davidson-Arnott RG, Bauer BO, Namikas SL, Ollerhead  
714 J (2009) Responses of three-dimensional flow to variations in the angle of  
715 incident wind and profile form of dunes: Greenwich dunes, prince edward  
716 island, canada. *Geomorphology* 105:127–138
- 717 Weaver C, Wiggs G (2011) Field measurements of mean and turbulent airflow  
718 over a barchan sand dune. *Geomorphology* 128:32–41
- 719 Wiggs G, Livingstone I, Warren A (1996) The role of streamline curvature in  
720 sand dune dynamics: evidence from field and wind tunnel measurements.  
721 *Geomorphology* 17:29–46
- 722 Wiggs G, Bullard J, Garvey B, Castro I (2002) Interactions between airflow  
723 and valley topography with implications for aeolian sediment transport.  
724 *Physical Geography* 23:366–380
- 725 Zhang C, Li Q, Zhou N, Zhang J, Kang L, Shen Y, Jia W (2016) Field obser-  
726 vations of wind profiles and sand fluxes above the windward slope of a sand  
727 dune before and after the establishment of semi-buried straw checkerboard  
728 barriers. *Aeolian Res* 20:59–70
- 729 Zilker DP, Hanratty TJ (1979) Influence of the amplitude of a solid wavy wall  
730 on a turbulent flow. part 2. separated flows. *J Fluid Mech* 90:257–271
- 731 Zilker DP, Cook GW, Hanratty TJ (1977) Influence of the amplitude of a solid  
732 wavy wall on a turbulent flow. part 1. non-separated flows. *J Fluid Mech*  
733 82:29–51

734           **Local wind regime induced by giant linear dunes**  
 735           — Supplementary Material —

736   **C. Gadal\* · P. Delorme · C. Narteau · G.F.S. Wiggs · M. Baddock ·**  
 737   **J.M. Nield · P. Claudin**

738

739   \* Institut de Mécanique des Fluides de Toulouse, Université de Toulouse Paul  
 740   Sabatier, CNRS, Toulouse INP-ENSEEIHT, Toulouse, France.

741   cyril.gadal@imft.fr

742   **1. Shear velocity and calibration of the hydrodynamical roughness**

743   As the regionally predicted and locally measured velocities are available at  
 744   different heights, we can not compare them directly. We therefore convert all  
 745   velocities into shear velocities  $u_*$ , characteristic of the turbulent velocity profile  
 746   (Spalding 1961; Stull 1988):

$$\frac{u(z)}{u_*} = \frac{1}{\kappa} \ln \left( \frac{z}{z_0} \right), \quad (15)$$

747   where  $z$  is the vertical coordinate,  $\kappa = 0.4$  the von Kármán constant and  $z_0$  the  
 748   hydrodynamic roughness. Several measurements of hydrodynamic roughnesses  
 749   are available (Raupach 1992; Bauer et al. 1992; Brown et al. 2008; Nield et al.  
 750   2014). In the absence of sediment transport, it is governed by the geometric  
 751   features of the bed (Flack and Schultz 2010; Pelletier and Field 2016). When  
 752   aeolian saltation occurs, it is rather controlled by the altitude of Bagnold's  
 753   focal point (Durán et al. 2011; Valance et al. 2015), which depends on the  
 754   wind velocity and grain properties (Sherman and Farrell 2008; Zhang et al.  
 755   2016; Field and Pelletier 2018). Whether associated with geometric features  
 756   or with sediment transport, its typical order of magnitude is the millimetre  
 757   scale on sandy surfaces.

758   We do not have precise velocity vertical profiles to be able to deduce an  
 759   accurate value of  $z_0$  in the various environments of the meteorological stations  
 760   (vegetated, arid, sandy). Our approach is to rather select the hydrodynamic  
 761   roughness which allows for the best possible matching between the regionally  
 762   predicted and locally measured winds, i.e. minimising the relative difference  $\delta$   
 763   between the wind vectors of both datasets:

$$\delta = \frac{\sqrt{\langle \|\mathbf{u}_{*,\text{era}} - \mathbf{u}_{*,\text{station}}\|^2 \rangle}}{\sqrt{\langle \|\mathbf{u}_{*,\text{era}}\| \rangle \langle \|\mathbf{u}_{*,\text{station}}\| \rangle}}, \quad (16)$$

764   where  $\langle \cdot \rangle$  denotes time average. This parameter is computed for values of  $z_0$   
 765   in ERA5-Land analysis ranging from  $10^{-5}$  m to  $10^{-2}$  m for the four different  
 766   stations. Note that for the North Sand Sea and South Sand Sea stations, where  
 767   the giant dunes feedback presumably affect the wind, we take into account the  
 768   non-deflected winds only in the calculation of  $\delta$  (with a  $15^\circ$  tolerance).

As shown in Online Resource Fig. S4, the minimum values of  $\delta$  in the space  $(z_0^{\text{ERA5Land}}, z_0^{\text{local}})$  form a line. We thus set the roughness in the ERA5-Land analysis to the typical value  $z_0 = 10^{-3}$  m, and deduce the corresponding ones for the local stations. It leads to 2.7, 0.8, 0.1 and 0.5 mm for the Adamax, North Sand Sea, Huab and South Sand Sea stations, respectively. Importantly, this approach somewhat impacts the calculation of the shear velocities, but not that of the wind directions. As such, most of our conclusions are independent of such a choice. However, it may affect the magnitude of the wind velocity attenuation/amplification in flow confinement situations.

## 2. Computation of the ABL characteristics

The estimation of the non-dimensional numbers associated with the ABL requires the computation of representative meteorological quantities. In arid areas, the vertical structure of the atmosphere can be approximated by a well mixed convective boundary layer of height  $H$ , topped by the stratified free atmosphere (Stull 1988; Shao 2008). In this context, one usually introduces the virtual potential temperature  $T_{\text{vp}}$ , which is a constant  $T_0$  inside the boundary layer, and increases linearly in the FA (Online Resource Fig. S11a):

$$T_{\text{vp}}(z) = \begin{cases} T_0 & \text{for } z \leq H, \\ T_0 \left( 1 + \frac{\Delta T_{\text{vp}}}{T_0} + \frac{N^2}{g}(z - H) \right) & \text{for } z \geq H, \end{cases} \quad (17)$$

where  $\Delta T_{\text{vp}}$  is the temperature discontinuity at the capping layer and  $N = \sqrt{g\partial_z T_{\text{vp}}/T_0}$  is the Brunt-Väisälä frequency, characteristic of the stratification. Note that, under the usual Boussinesq approximation, temperature and air density variations are simply related by  $\delta T_{\text{vp}}/T_0 \simeq -\delta\rho/\rho_0$  (see Online Resource of Andreotti et al. (2009)), so that  $N$  can equivalently be defined from the density gradient as next to Eq. 1.

The ERA5 dataset provides vertical profiles of the geopotential  $\phi$ , the actual temperature  $T$  and the specific humidity  $\eta$  at given pressure levels  $P$ . The vertical coordinate is then calculated as:

$$z = \frac{\phi R_t}{g R_t - \phi}, \quad (18)$$

where  $R_t = 6371229$  m is the reference Earth radius and  $g = 9.81$  m s<sup>-2</sup> is the gravitational acceleration. One also computes the virtual potential temperature as:

$$T_{\text{vp}} = T \left[ 1 + \left( \frac{M_d}{M_w} - 1 \right) \eta \right] \left( \frac{P_0}{P} \right)^{R/C_p}, \quad (19)$$

where  $P_0 = 10^5$  Pa is the standard pressure,  $R = 8.31$  J/K is the ideal gas constant,  $C_p \simeq 29.1$  J/K is the air molar heat capacity, and  $M_w = 0.018$  kg/Mol

800 and  $M_d = 0.029 \text{ kg/Mol}$  are the molecular masses of water and dry air respectively.  
 801 The specific humidity is related to the vapour pressure  $p_w$  as

$$\eta = \frac{\frac{M_w}{M_d} p_w}{p - \left(1 - \frac{M_w}{M_d}\right) p_w}. \quad (20)$$

802 The ERA5 dataset also provides an estimate of the ABL depth  $H$ , based  
 803 on the behaviour of the Richardson vertical profile. This dimensionless num-  
 804 ber is defined as the ratio of buoyancy and flow shear terms, and can be  
 805 expressed as  $\text{Ri} = N^2 / (\partial_z u)^2$ . It vanishes in the lower well-mixed layer where  
 806  $T_{\text{vp}}$  is constant, and increases in the stratified FA. Following the method and  
 807 calibration of Vogelegang and Holtslag (1996); Seidel et al. (2012), the value  
 808  $\text{Ri}(z) \simeq 0.25$  has been shown to be a good empirical criterion to give  $z \simeq H$   
 809 within a precision varying from 50% for the shallower ABL (e.g. at night) to  
 810 20% for situations of stronger convection.

811 Examples of vertical profiles of the virtual potential temperature deduced  
 812 from ERA5 are shown in Online Resource Fig. S11a. For each of them, an  
 813 average temperature is computed below the ABL depth ( $z < H$ ), and a linear  
 814 function is fitted above, allowing us to extract the temperature jump  $\Delta T_{\text{vp}}$ .  
 815 Importantly, some profiles display a vertical structure that cannot be approx-  
 816 imated by the simple form (17) used here (Online Resource Fig. S11b). In  
 817 practice, we removed from the analysis all of those leading to the unphysical  
 818 case  $\Delta T_{\text{vp}} < 0$ . We have noticed that these ‘ill-processed’ profiles dominantly  
 819 occur in winter and are evenly spread across the hours of the day. Importantly,  
 820 they represent  $\simeq 12\%$  of the data only (Online Resource Fig. S11c,d), and we  
 821 are thus confident that this data treatment does not affect our conclusions.

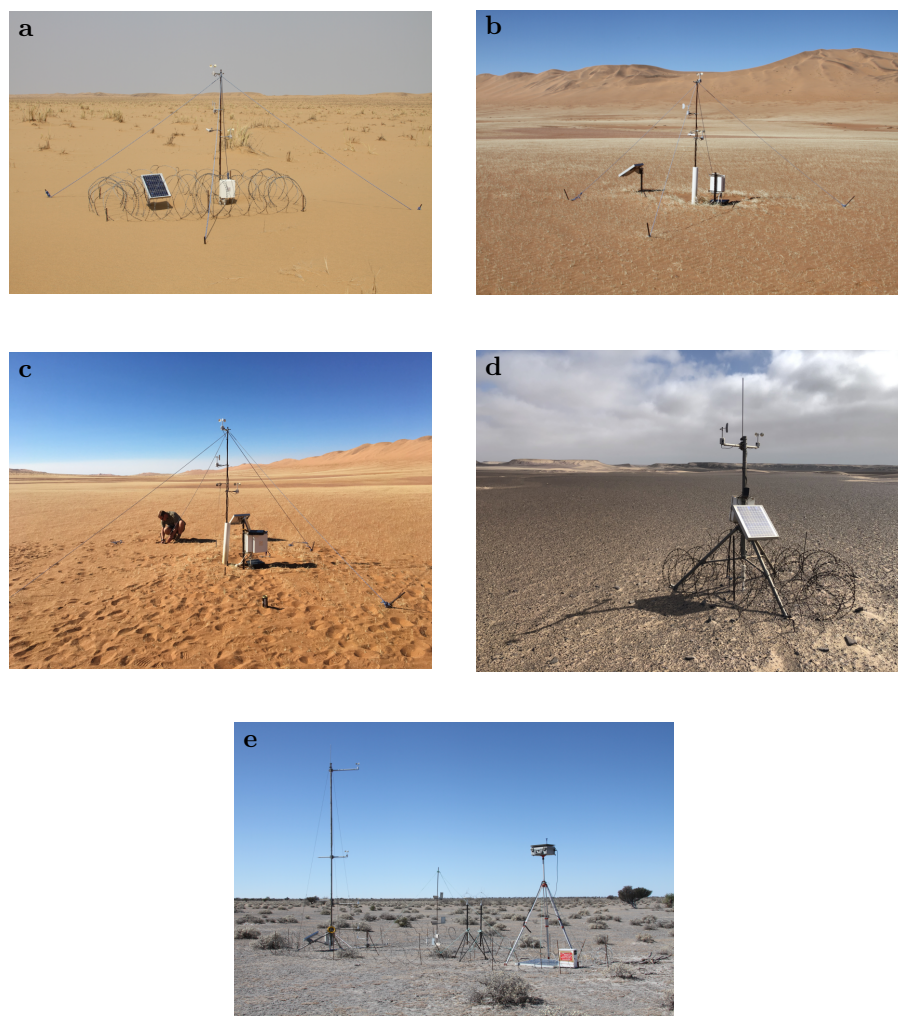


**Fig. S1** Photographs of the meteorological stations. **a:** South Sand Sea station. **b–c:** North Sand Sea station. **d:** Huab station. **e:** Adamax station.

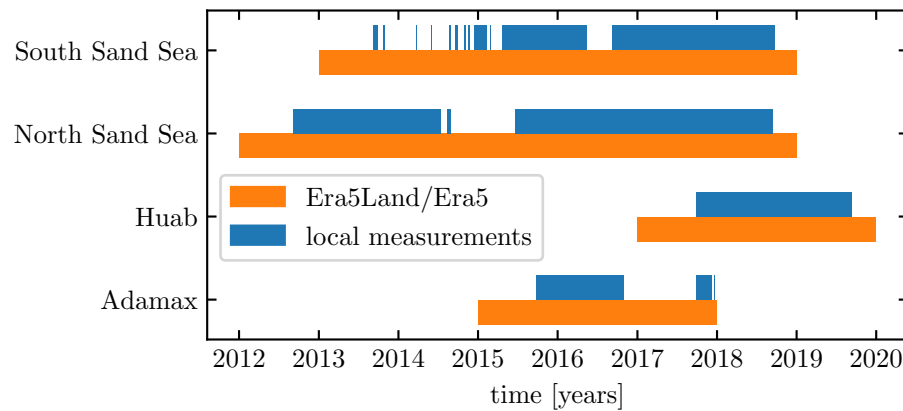


**Fig. S2** Gant chart representing the valid time steps for the two data sets, for all stations.

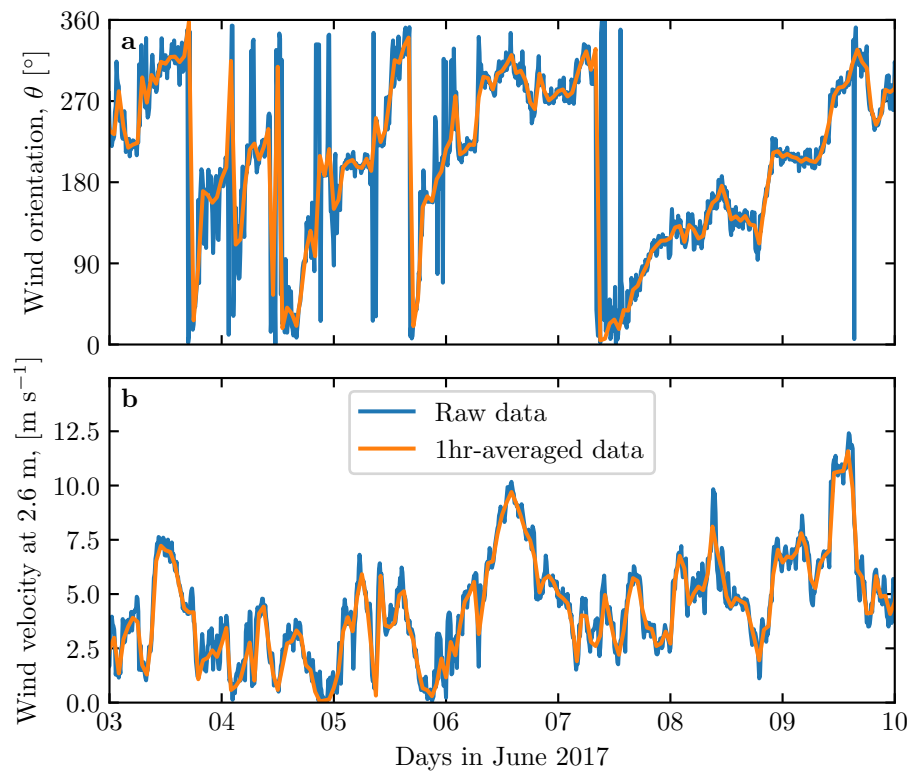


**Fig. S3** Comparison between raw local wind measurements, and hourly-averaged data for South Sand Sea station. **a:** wind direction. **b:** wind velocity at height 2.6 m.

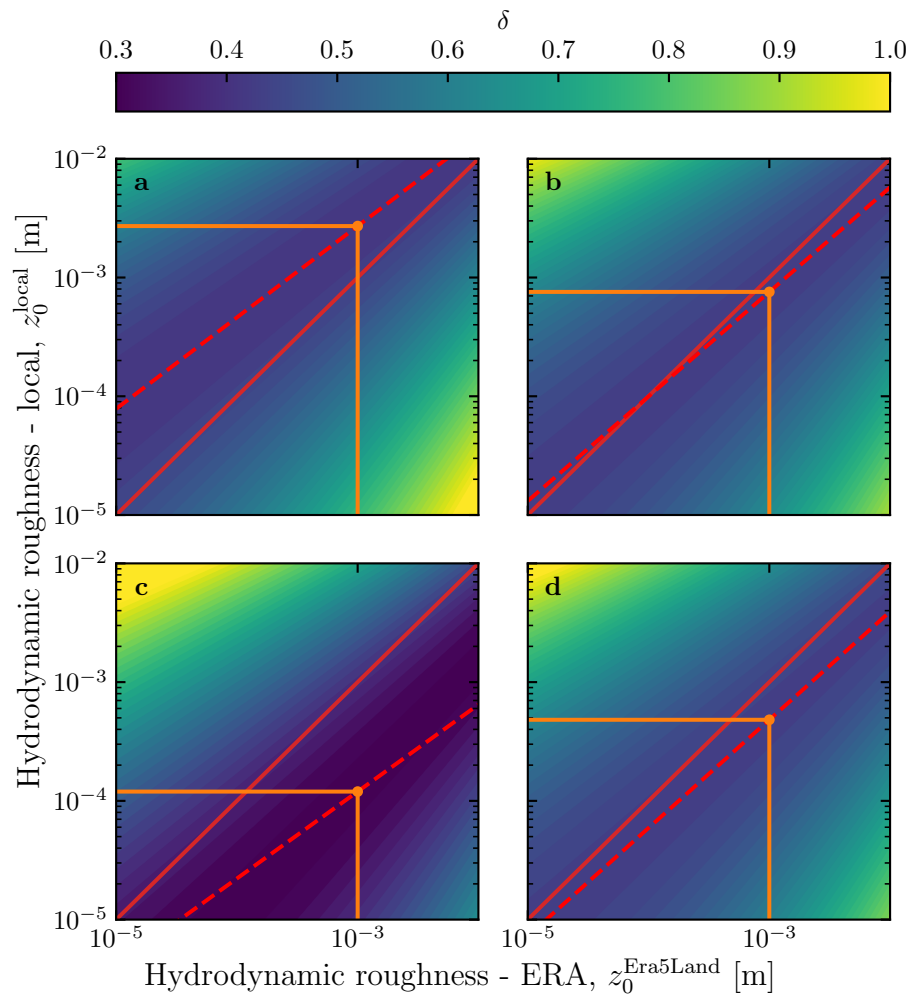


**Fig. S4** Calibration of hydrodynamic roughness. The parameter  $\delta$  (Eq. 16) quantifying the difference between local and predicted winds is shown in colorscale as a function of the hydrodynamic roughnesses chosen for the ERA5-Land and for local winds, for the (a) Adamax, (b) North Sand Sea, (c) Huab and (d) South Sand Sea stations. The red dashed and plain lines shows the minima of  $\delta$  and the identity line, respectively. The orange lines and dots highlight the chosen hydrodynamic roughnesses for the local winds deduced from setting  $z_0^{\text{ERA5Land}} = 1 \text{ mm}$ .

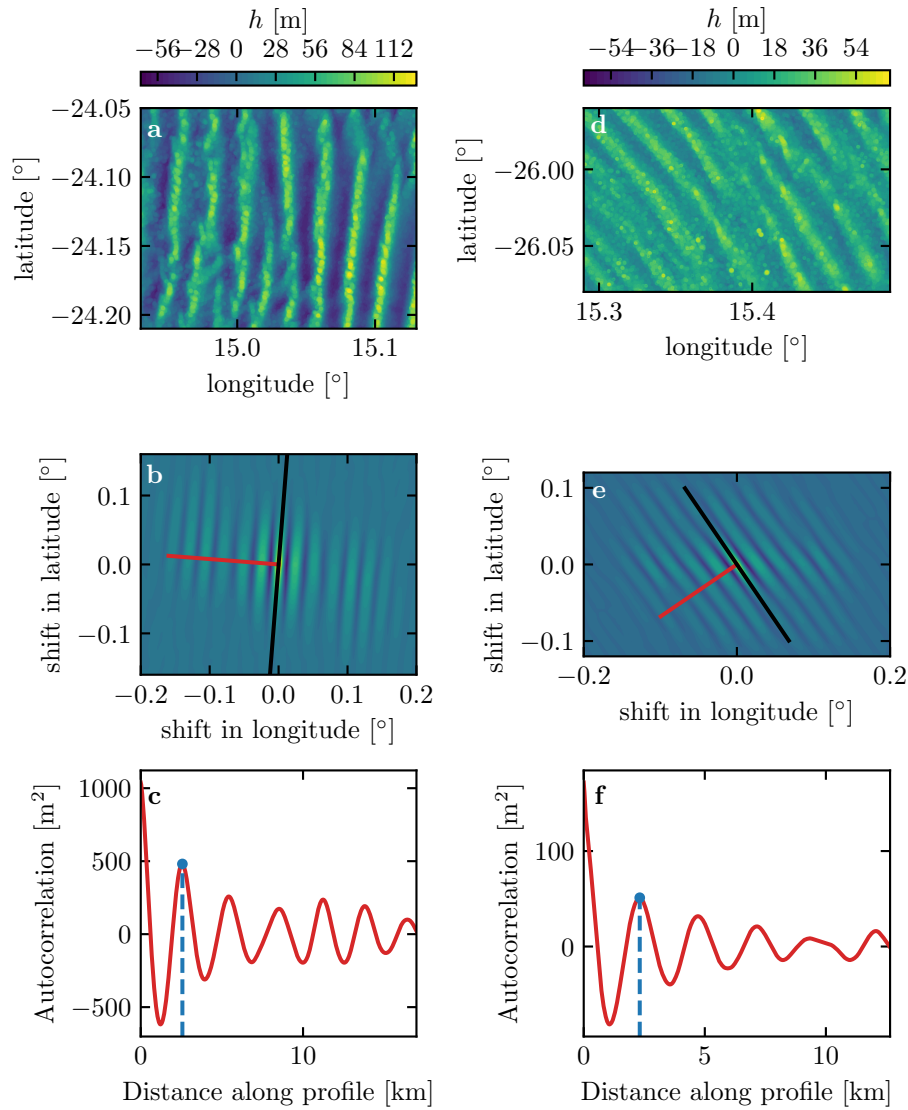


**Fig. S5** Analysis of the DEMs of the North Sand Sea (left column – panels **a**, **b**, **c**) and South Sand Sea (right column – panels **d**, **e**, **f**) stations. **a–d**: Bed elevation detrended by a fitted second order polynomial base-line. **b–e**: Autocorrelation matrix shown in colorscale. The black line shows the detected dune orientation, and the red line represents the autocorrelation profile along which the dune wavelength is calculated, displayed in **c–f**. The blue lines and dots show the first peak of the autocorrelation profile, whose abscissa gives the characteristic wavelength of the dune pattern.

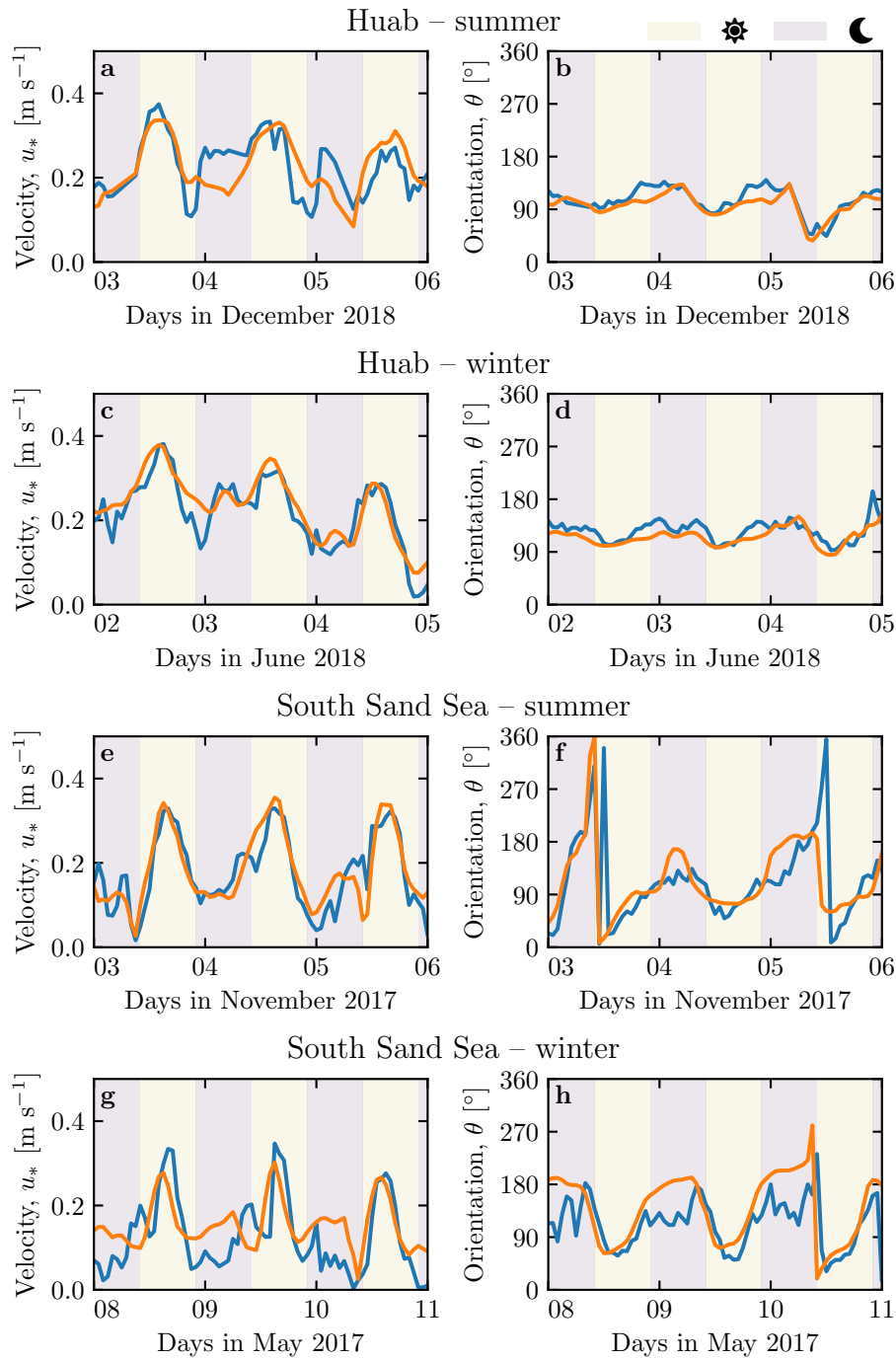


**Fig. S6** Temporal comparison between the wind data coming from the ERA5-Land climate reanalysis (orange lines) and from the local measurements (blue lines). Coloured swathes indicate day (between 1000 UTC and 2200 UTC) and night (before 1000 UTC or after 2200 UTC) **a–b**: Huab station in summer. **b–c**: Huab station in winter. **d–e**: South Sand Sea station in summer. **f–g**: South Sand Sea station in winter.

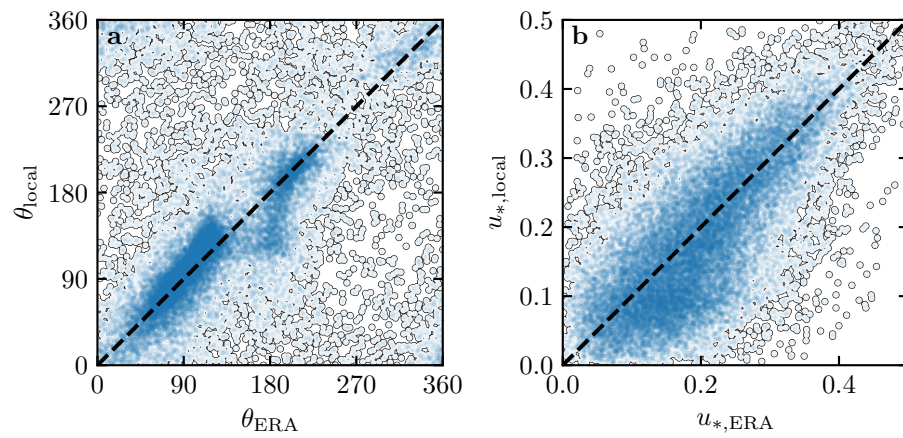


**Fig. S7** Statistical comparison of the wind orientation (a) and velocity (b) between the ERA5-Land dataset and the local measurements for the Huab and Adamax stations. Data point clustering around identity lines (dashed and black) provide evidence for agreement of the two sets.

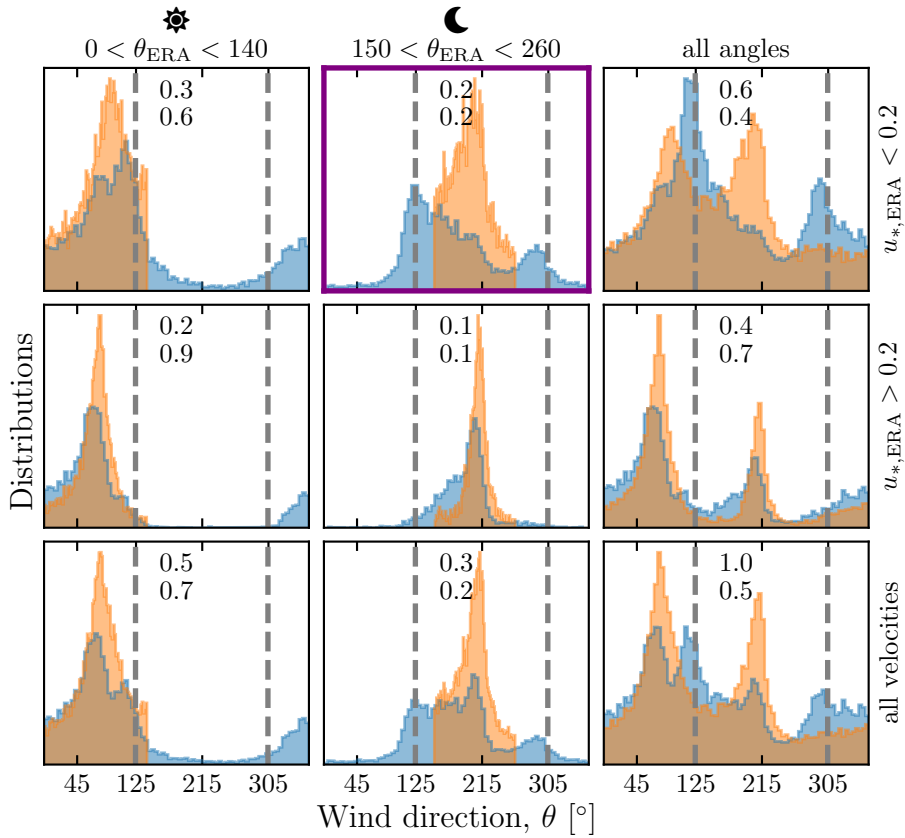


**Fig. S8** Distributions of wind direction at the South Sand Sea Station for the ERA5-Land climate reanalysis (orange) and the local measurements (blue) – equivalent of Fig. 3. In each subplot, both distributions are plotted from the same time steps, selected with constraints on the wind direction (columns) and/or wind velocity (rows) in the ERA5-Land dataset. The gray vertical dashed lines indicate the dune orientation. The numbers at the top centre give the percentage of time steps selected in each sub-range, as well as the percentage of them corresponding to the day (between 1000 UTC and 2200 UTC). The purple frame highlights the regime (small wind velocities, nocturnal summer wind) during which the wind data from both datasets differ.

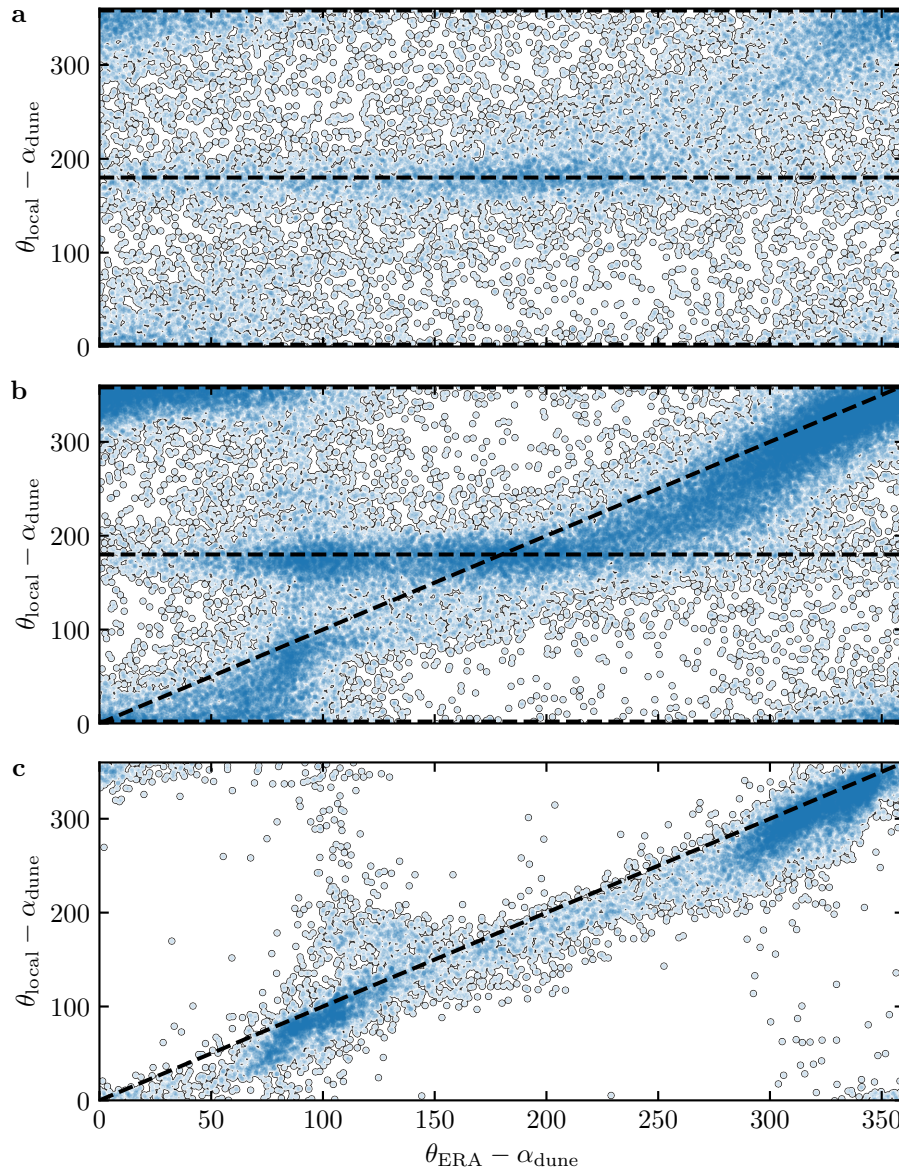


**Fig. S9** Statistical comparison of the wind orientation between the ERA5-Land dataset and the local measurements for the South Sand Sea and North Sand Sea stations, for different velocity ranges. **a:**  $u_{*,\text{ERA}} < 0.1 \text{ m s}^{-1}$ . **b:**  $0.1 < u_{*,\text{ERA}} \leq 0.25 \text{ m s}^{-1}$ . **c:**  $u_{*,\text{ERA}} \geq 0.25 \text{ m s}^{-1}$ . The measured dune orientations are subtracted to the wind orientation, which allows us to plot both stations on the same graph. Black dashed lines indicate locally measured orientations aligned with the dune crests (here 0°, 180° and 360° – panels a, b), as well as the identity lines (panels b, c).

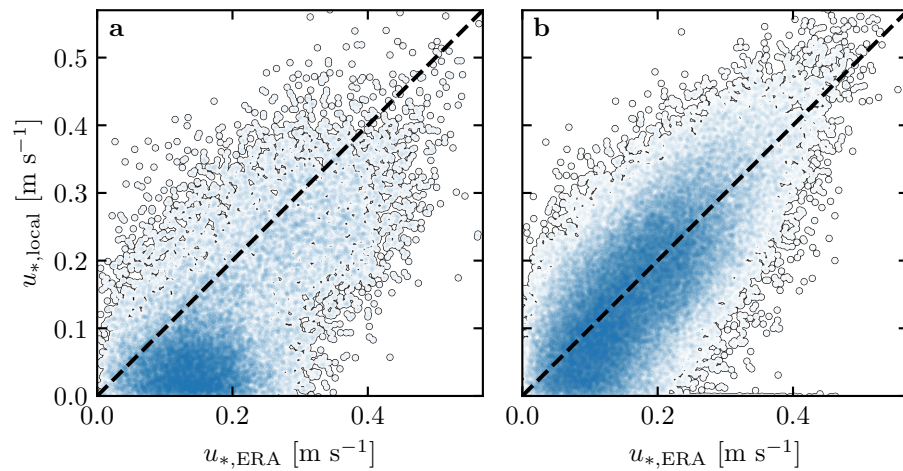


**Fig. S10** Statistical comparison of the wind velocity between the ERA5-Land dataset and the local measurements for the South Sand Sea and North Sand Sea stations. **a:** Nocturnal summer easterly wind. **b:** Diurnal southerly wind. Black dashed lines are identity lines. The angle ranges used to select diurnal and nocturnal summer winds are the same as those in Fig. 3 and Online Resource Fig. S8.

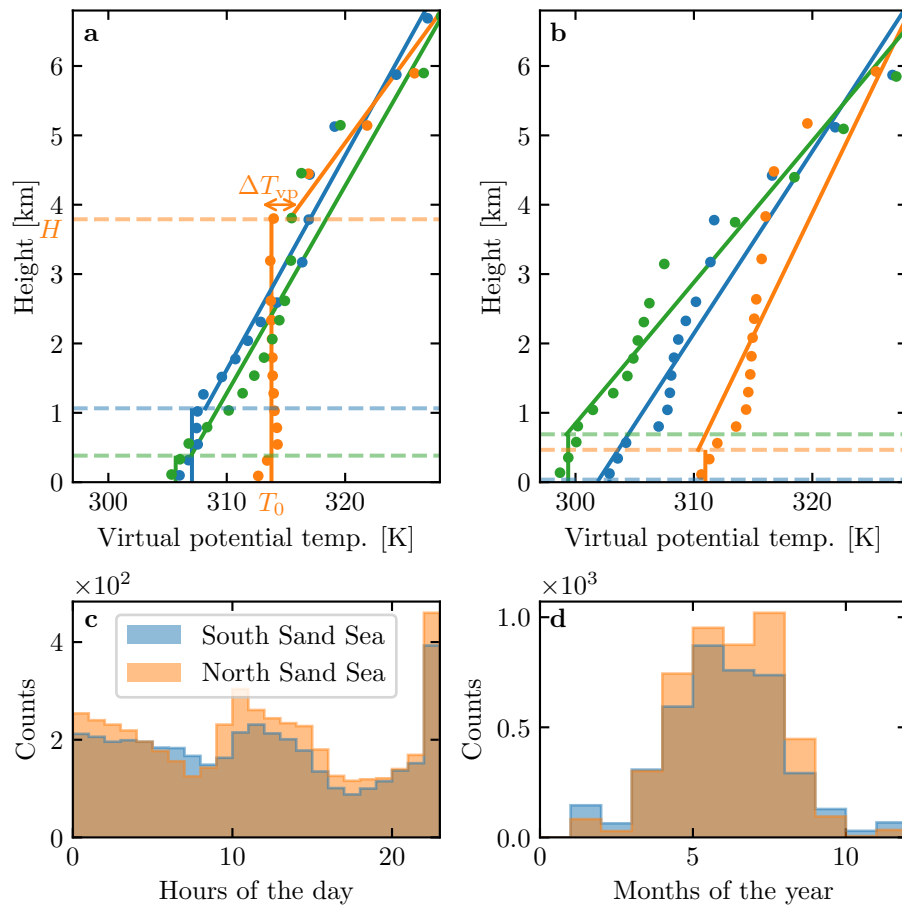


**Fig. S11** **a:** Vertical profiles of the virtual potential temperature at three different times (blue: 29/11/2012 - 1100 UTC, orange: 21/03/2017 - 1200 UTC, green: 21/03/2017 - 2000 UTC) at the South Sand Sea station. Dots: data from the ERA5 reanalysis. Dashed lines: boundary layer height given by the ERA5 reanalysis. Plain lines: vertical (ABL) and linear (FA) fits to estimate the quantities displayed in Online Resource Fig. S12. **b:** Examples of ill-processed vertical profiles at three different times (blue: 2/12/2013 - 2300 UTC, orange: 20/03/2017 - 0000 UTC, green: 14/07/2017 - 1400 UTC) at the South Sand Sea station. **c:** Hourly distribution of ill-processed vertical profiles. **d:** Monthly distribution of ill-processed vertical profiles.

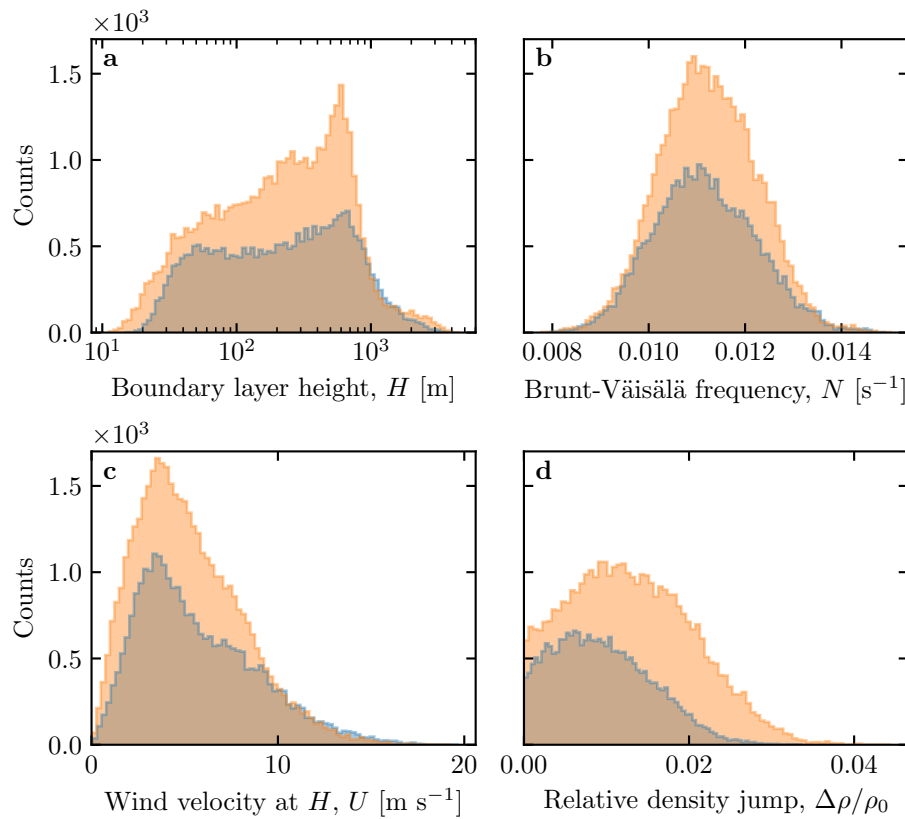


**Fig. S12** Distributions of the meteorological parameters resulting from the processing of the ERA5-Land data for the South Sand Sea (blue) and the North Sand Sea (orange) stations.

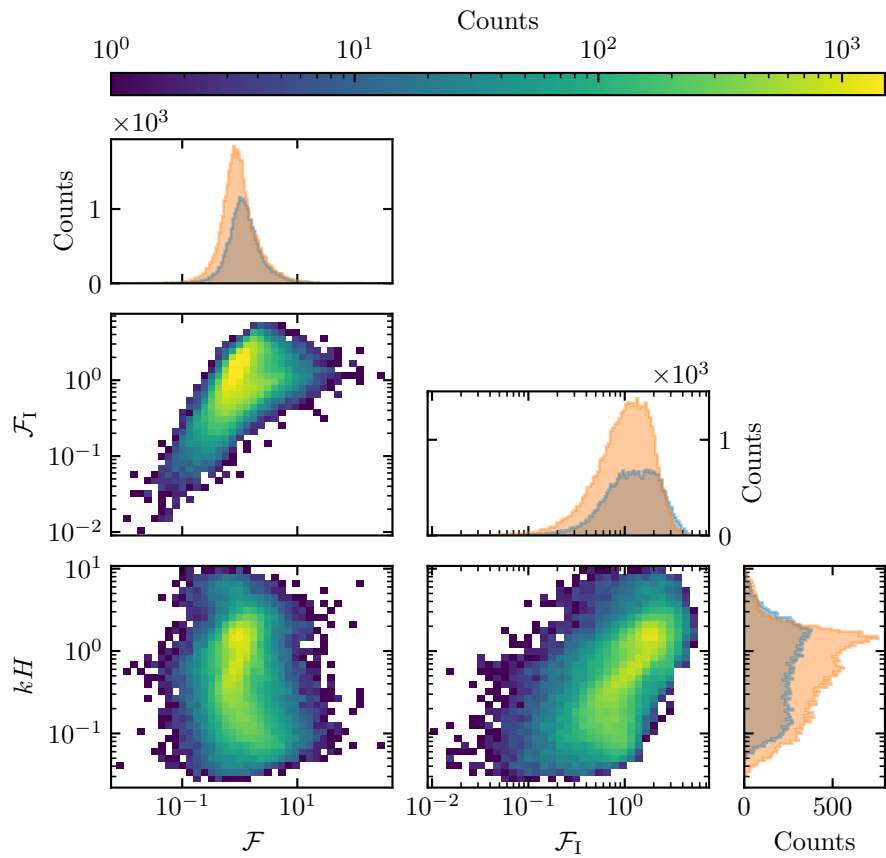


**Fig. S13** Non-dimensional parameters distributions. For the marginal distributions, the orange correspond to the South Sand Sea station, and the blue to the North Sand Sea station.

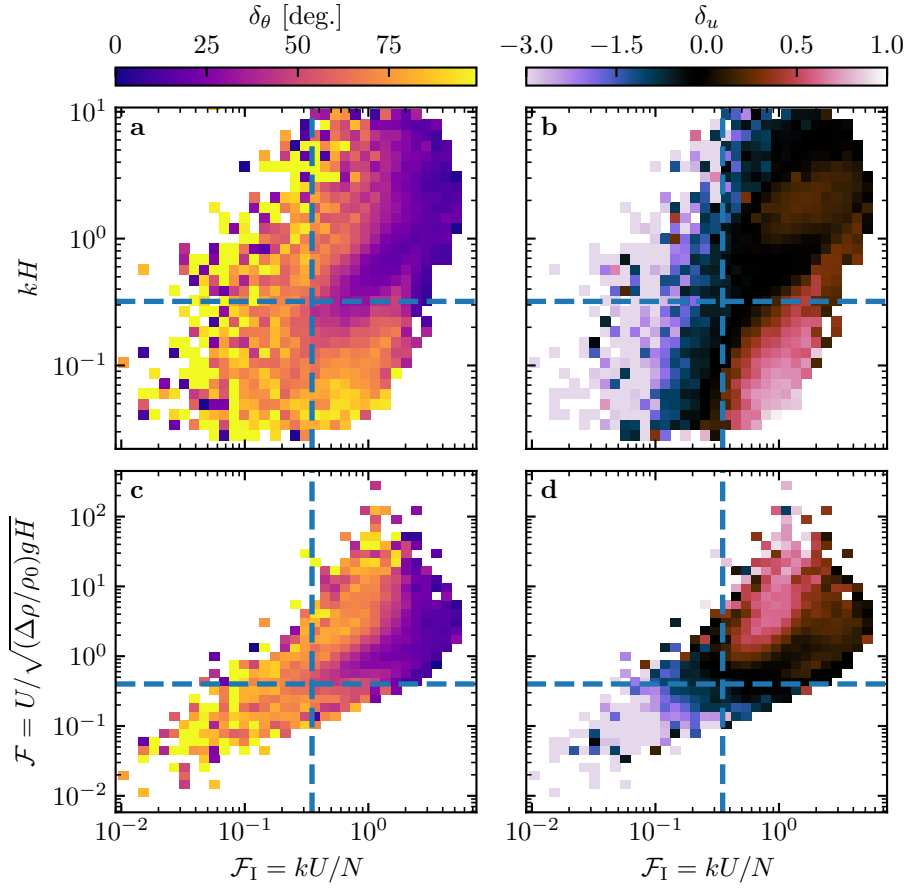


**Fig. S14** Regime diagrams of the wind deviation  $\delta_\theta$  and relative attenuation/amplification  $\delta_u$  in the spaces  $(\mathcal{F}_I, kH)$  and  $(\mathcal{F}_I, \mathcal{F})$ , containing the data from both the North Sand Sea and South Sand Sea stations. Blue dashed lines empirically delimit the different regimes. The point density in each bin of the diagrams is shown in Online Resource Fig. S13 – 95% of the data occur in the range  $-1 < \delta u < 1$ . The similar regime diagrams in the space  $(\mathcal{F}, kH)$  are shown in Fig. 5.

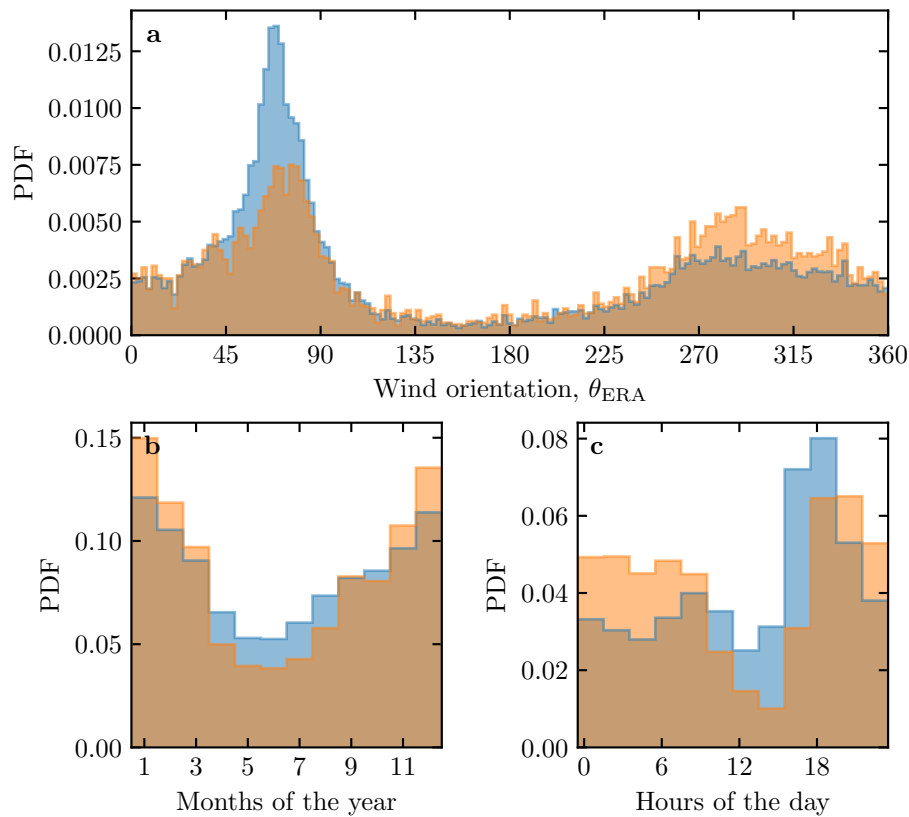


**Fig. S15** Normalized distributions of amplified velocities for the North Sea (blue:  $\delta_u < 0$ , orange:  $\delta_u < -0.5$ ). **a:** Angular distributions. **b:** Monthly distributions. **c:** Hourly distributions.

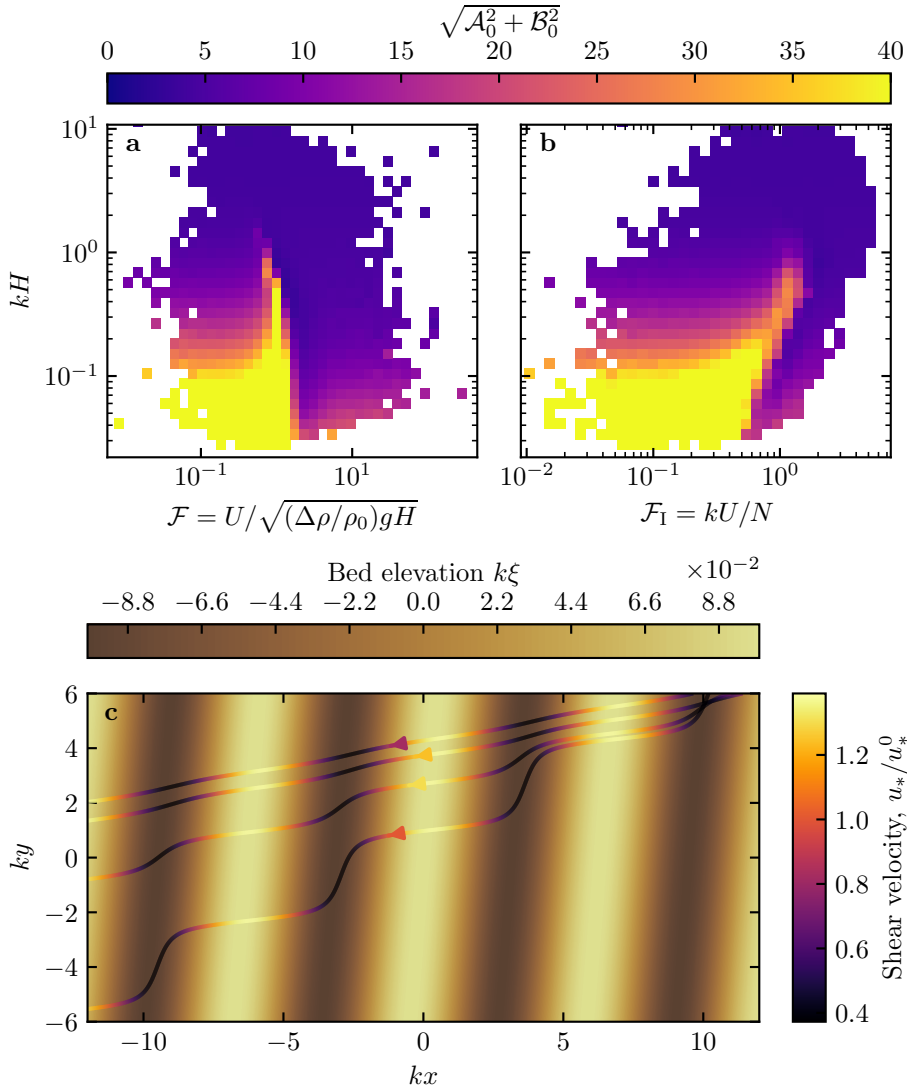


**Fig. S16** Computation of the flow disturbance with the linear model of Andreotti et al. (2009). **a** and **b** Magnitude of the hydrodynamic coefficients  $A_0$  and  $B_0$ , calculated from the values of the non-dimensional numbers corresponding to the ERA5-Land time series presented in Figs. 4 and 5. **c** Shear velocity streamlines over sinusoidal ridges of amplitude  $k\xi_0 = 0.1$  and for increasing values of  $\sqrt{A_0^2 + B_0^2}$ . From the upper to the lower streamline, values of  $(kH, \mathcal{F}, \mathcal{F}_I, A_0, B_0, \sqrt{A_0^2 + B_0^2})$  are  $(1.9, 0.6, 1.5, 3.4, 1.0, 3.5)$ ,  $(1.5, 0.3, 0.4, 4.8, 1.4, 5.0)$ ,  $(0.1, 3.5, 1.0, 8.6, 0.1, 8.6)$ ,  $(0.5, 0.05, 0.04, 9.6, 2.5, 9.9)$ .